Amer Orucevic

Underwater snake robots in vortex wakes:

Energy harvesting and position control

NTNU

Norwegian University of
Science and Technology

Amer Orucevic

Underwater snake robots in vortex wakes:

Energy harvesting and position control

Master's thesis in Cybernetics and robotics
Supervisor: Jan Tommy Gravdahl
June 2020

Norwegian University of Science and Technology
Faculty of Information Technology and Electrical Engineering
Department of Engineering Cybernetics

NTNU
Kunnskap for en bedre verden

NTNU
Norges teknisk-naturvitenskapelige
universitet

Fakultet for informasjonsteknologi,
matematikk og elektroteknikk
Institutt for teknisk kybernetikk

MSc thesis assignment

Name of the candidate: Amer Orucevic
Subject: Engineering Cybernetics
Title: Underwater snake robots in vortex wakes: Energy harvesting and
                           position control

Background:

This assignment is concerned with the concept of utilizing fluid vortices for energy harvesting purposes by articulated intervention underwater vehicles (AIAUV).

Tasks:

1. Perform a literature study on the concept of energy harvesting from fluid vortices
2. By using [1] as inspiration, develop models of articulated bodies, that is passive swimmers, in a vortex wake
3. Develop a simulator for the models developed in Task 2. Study the energy harvesting properties and discuss the results.
4. Design and simulate a control system enabling an AIAUV to hold its position in a vortex wake

To be handed in by: 29/6-2020
Co-supervisor: Professor Kristin Y. Pettersen

Jan Tommy Gravdahl
Professor, supervisor

[1] Bernier, C., Gazzola, M., Ronsse, R. and Chatelain, P. (2019). Simulations of propelling and energy harvesting articulated bodies via vortex particle-mesh methods, Journal of Computational Physics 392: 34–55.

Abstract

This thesis investigates how energy can be harvested from the wake of a bluff body to achieve energy autonomy for an articulated intervention autonomous underwater vehicle (AIAUV) by using undulatory motions.

The relevant literature concerning energy harvesting, simulation models of objects downstream from a cylinder and control methods regarding the motion of underwater snake robots (USR) is reviewed. Then, the necessary fluid mechanics theory is presented.

The equations of motion for four submerged bodies are then derived. The first model is a double pendulum, consisting of two rectangular links connected by a rotational spring and damper, where the first link is connected to a cylinder. The second model is a square with smoothed edges constrained by springs and dampers connected to a cylinder and the lower end wall. The third model is an elliptical three link pendulum where the links are connected by rotation springs and dampers, the first link is immovable to constrain the horizontal motion of system. The final model is an elliptical three link pendulum where the links are connected with linear springs and the first link is connected to a cylinder with a spring.

The first three models are then implemented in COMSOL Multiphysics, while the last model is implemented in a simulator that has been computationally verified in related work and is used to assess the reliability of the models developed. The simulations show that all the models are capable of harvesting energy from the dampers, and the horizontal and vertical displacements observed for all models are similar, indicating that the results are reliable. However, the angular velocity varies between the models, implying that assessing the reliability of these results has to be investigated in future work.

Finally, a controller for holding a desired position in the presence of constant disturbances, while maintaining an undulatory gait is proposed. The performance of the controller is investigated through three simulation studies, where the position error approaches zero as it oscillates with a negligible amplitude.

Sammendrag

Denne oppgaven utforsker mulighetene for bruk av bølgebevegelser til energisamling. Ved å utnytte virvlene som oppstår bak en sylinder er målet å oppnå energiautonomitet i artikulerte intervensjons-autonome undervannsfarkoster (AIAUV-er).

Den relevante litteratur relatert til energisamling, simuleringsmodeller og posisjonskontroll av undervannsslangeroboter (USR-er) er gjennomgått. Deretter blir nødvendig teori vedrørende fluiddynamikk presentert.

Videre er bevegelsesligningene for fire nedsenkede objekter beregnet. Den første modellen består av en dobbel pendel med ledd formet som rektangler. Disse er festet til en sylinder med en fjær og demper. Den andre modellen er et kvadrat med avrundede hjørner. Bevegelser blir her begrenset ved å koble kvadratet til en vegg og i tillegg en sylinder ved bruk av horisontale og vertikale fjærer og dempere. Den tredje modellen er en elliptisk pendel med tre ledd. Disse leddene er forbundet med roterende fjærer og dempere. For å begrense horisontal bevegelse er det første leddet gjort ubevegelig. Den siste modellen er også en elliptisk pendel bestående av tre ledd. Leddene er her koblet med fjærer. Det første leddet er i tillegg koblet til en sylinder med en fjær.

De tre første modellene blir deretter implementert i COMSOL Multiphysics. For å vurdere om resultatene er troverdige, ble den siste modellen implementert i en simulator som har blitt verifisert i relaterte studier. Resultatene viser at alle modellene med dempere kan samle energi fra omgivelsene. Den horisontale og vertikale bevegelsen er lignende for begge simuleringsmetoder, og disse resultatene er derfor troverdige. Vinkelhastighetene varierer mye for de ulike modellene og impliserer at videre studier kreves for å vurdere troverdigheten av de målte vinkelhastighetene.

Til slutt blir det foreslått en type kontroller som kan holde en bestemt posisjon i omgivelsene på tross av konstante forstyrrelser. Dette ved å bruke bølgebevegelser for fremdrift. Kontrollen blir så vurdert gjennom tre simuleringsstudier der posisjonsfeilen går mot null og oscillerer med en neglisjerbar amplitude.

Preface

This thesis is submitted as a partial fullfilment of the requirements for the degree of Master of Science in Cybernetics at the Norwegian University of Science and Technology (NTNU). The work presented in this thesis has been carried out under the supervision of Professor Jan Tommy Gravdahl and co-supervisor Professor Kristin Y. Pettersen, at the department of Engineering Cybernetics, NTNU.

The models simulated in this thesis were developed by the use of COMSOL Multiphysics, which is a general-purpose simulation software for modeling designs, devices and processes in all fields of engineering.

A simulator developed by Assistant Professor Mattia Gazzola and his team at the Univerisity of Illinois Urbana-Champaign, was also used to simulate a model for comparison with the COMSOL models developed.

The MATLAB simulator used to simulate the motions of a USR with the proposed position hold controller, were developed by Dr. Anna Kohl and Dr. Eleni Kelasidi, during their time as PhD Candidates at NTNU.

Unless otherwise stated, all figures and illustrations have been created by the auther of this thesis.

Acknowledgements

Contents

Abbreviations

AIAUV articulated intervention autonomous underwater vehicle

AUV Automated underwater vehicle

BSD Block with double springs and dampers

CFD Computational fluid dynamics

CG Centre of Gravity

DP Double pendulum with spring and damper

FEM Finite element method

FSI Fluid-structure interaction

FVM Finite volume method

ILOS Integral Line-Of-Sight

LOS Line-Of-Sight

MBS Multi-Body System

MTLS Modified three linked swimmer

ROV Remotely operated vehicles

TLS Three linked swimmer

USR underwater snake robot

List of Tables

List of Figures

Chapter 1

Introduction

This introductory chapter will present the motivation behind the thesis and a description of the problems to be solved. Then the contributions of this thesis are presented.

1.1 Motivation

Many global challenges, such as global warming, food and water security, renewable energy, transport, understanding the ecosystem, accessing raw materials or biodiversity are all dependent on our understanding of the ocean. Through the evolution of remotely operated vehicles (ROVs) and autonomous underwater vehicles (AUVs) new possibilities for exploring the seas have emerged and the need for direct human interaction is decreasing. However, many tasks still require precision and mobility to traverse unyielding areas. The articulated intervention underwater vehicle (AIAUV) is an advancement of the underwater snake robots (USR), with longitudinal and tunnel thrusters along the body. The AIAUV has the ability to operate as a vehicle and manipulator, while maintaining the flexibility of an USR. Some AIAUVs have been developed to permanently operate underwater, but it still requires charging stations and charging infrastructure. The battery capacities of these devices is a limiting factor for the area of operation. Therefore a robotic system with extreme endurance in both time and space, with the ability to traverse long distances while accessing narrow spaces and interacting with the environment, would be a major step forward in our attempts to learn from the sea.

To achieve a larger operational area, it is necessary to develop methods for the AIAUV to extract energy from the oceans. The Kàrmàn vortex street that forms when bluff bodies are placed in a stream might be a possible solution for achieving

hyper-effective propulsion for USRs and AIAUVs.

This requires the development of a simulation model that captures the fluid-structure interaction (FSI) between a submerged object and the vortex street. In this thesis four models are developed to study how such a simulation might be achieved for more complex swimmers such as the AIAUV.

1.2   Problem description

The AIAUV has the unique property that it can operate similarly to an USR. By inducing a sinusoidal undulation in the AIAUV a forward propulsion can be achieved as shown by Kohl et al. (2015b). The Kàrmàn vortex street consists of vortices that are shed from a bluff body in an asymmetric pattern, which might be used to create these undulations in the AIAUV, and generate forward propulsion by using less energy, and potentially without using any energy.

To study how this might be done, it is necessary to extend simulation models of the AIAUV to simulate a vortex wake, while capturing how the AIAUV interacts with the fluid and how this might change the environment. However, this requires the use of computational fluid dynamics (CFD) solvers, which are time consuming and very computationally heavy to run.

The goal of this thesis is to investigate how such a model can be implemented, by developing and studying simplified models of passive submerged objects in the wakes of cylinders in a two-dimensional environment. The study includes observations of how the different swimmers and shapes affect the simulation results and computational time, while also investigating if energy from the vortex wake can be harvested at some capacity. To evaluate if the results are reliable, a model is implemented and numerically studied with the simulator developed and verified through extensive simulation studies in Gazzola et al. (2011).

To achieve hyper-effective propulsion it is also necessary for the AIAUV to be capable of tracking bluff bodies while keeping a desired distance with an sinusoidal gate. In this thesis a controller for position holding for USRs is implemented and studied through simulations. This control algorithm might be extended in future work to attain the desired tracking for AIAUVs in the wake of moving bluff bodies.

1.3   Contributions

The main contributions of the works presented in this thesis are:

- A literature review of previous works concerning energy harvesting, simulation of Von Kàrmàn vortex streets with submerged bodies downstream and position control of USRs

- Implementing a simulation environment in COMSOL Multiphysics with a vortex wake behind a cylinder.

- Deriving the equations of motion for four passive swimmers, and implementing three of these in COMSOL Multiphysics, and the fourth model in the simulator presented and verified with extensive simulations studies in Gazzola et al. (2011).

- A simulation study where the models implemented in COMSOL Multiphysics are studied to investigate how energy can be harvested and how the different structures interact with the vortex street.

- A comparison between the models implemented in COMSOL Multiphysics and the model implemented in the simulator developed in Gazzola et al. (2011).

- By using the Integral line-of-sight (ILOS) guidance law presented in Kohl et al. (2016) and the simplified model for USRs as developed in Kelasidi, Pettersen and Gravdahl (2014), later extended by Kohl et al. (2015b) and Kohl et al. (2015a), a controller for holding a constant position in the presence of currents by using lateral undulation for forward propulsion is suggested.

- A simulation study for evaluating the performance and limitations of the proposed position hold controller with the following scenarios: (1) only constant currents in the horizontal direction, (2) constant currents in both horizontal and vertical direction and (3) when the horizontal position is reached before the vertical position with constant disturbances in both directions.

1.4 Outline

This thesis is divided into nine chapters and one appendix as described below:

Chapter 2 Presents some of the relevant literature covering topics in energy harvesting, simulation modelling of Von Kàrmàn vortex streets with submerged bodies downstream and position control for USRs.

Chapter 3 An overview of the relevant fluid mechanics theory is presented. First the Navier-Stokes equations are presented, then the Von Kàrman vortex wake

is discussed. Then the method of simulating the fluid-structure interaction as presented in Coquerelle and Cottet (2008), Gazzola et al. (2011) and Bernier et al. (2018) is presented. Finally the finite element method (FEM) is discussed.

Chapter 4 The equations of motion for four models are derived using the Euler-Lagrange equations. First the relevant theory is presented, then the equations of motion for the following models are derived:

- A double pendulum connected to a cylinder with a spring and damper.

- A block connected to a cylinder and to the lower-end wall with springs and dampers.

- A three link swimmer, where the first link is immovable.

- A three link swimmer connected to the cylinder with a spring, where the links are separated and connected with springs to each other.

Chapter 5 The implementation if the COMSOL Multiphysics simulations are presented, then the implementation details using the simulator presented in Gazzola et al. (2011) are discussed.

Chapter 6 The relevant theory and method for developing a controller to achieve a desired position with a USR is presented. First a simplified control oriented model of a USR is shown, then the ILOS guidance law developed in Kohl et al. (2016) is discussed. Finally the ILOS guidance law with minor modifications is combined with a PID controller for position hold by lateral undulations is presented.

Chapter 7 The results from the simulation studies are presented, then the results are discussed. First the results for the COMSOL models are presented and discussed. Then the results for the fourth model simulated with the simulator developed in Gazzola et al. (2011) are presented and compared to the COMSOL models.

Chapter 8 The position hold controller developed in Chapter 6 is studied through a simulation study. First the simulation details are presented, then the results for each case study is shown. Finally the results are discussed and compared.

Chapter 9 A conclusion is drawn from the results and discussions in previous chapters, then a suggestion for future work is given.

Appendix A Equations used for deriving the equations of motion that are not included in the main body for better readability are presented.

Chapter 2

Literature review

This chapter reviews some of the relevant work on energy harvesting, simulation models for objects in the wake of bluff bodies and controllers for USRs.

2.1   Energy harvesting

Wave energy conversion (WEC) from ocean waves has been investigated with several approaches as mentioned in Ozkop and Altas (2017). Although the potential for WEC is huge, large-scale deployment has not happened due to challenges such as mechatronic complexity and wear and tear on mechanisms due to large forces in the wave zone. Floating surface attenuators, which are investigated in Henderson (2006), are promising devices, but they are exposed to large forces, resulting in deterioration and damage over time.

Energy harvesting for snake-like structures in vortex wakes behind bluff bodies has been studied with promising results. In Allen and Smits (2001) four piezoelectric membranes were placed in the wakes of a bluff bodies, where two different configurations of bluff bodies were used. it was observed that the snake-like structures were able to exhibit lock-in behavior to the bluff body shedding, which is a requirement for achieving optimal coupling. Lock-in behavior means that the frequency of cross-flow oscillations and vortex shedding coincide, at a frequency close to the cylinders natural frequency. This results in a resonance condition where the membrane has a minimal damping effect on the vortex street. The study continues by investigating how different Reynolds numbers Re affect the membranes behavior. The Reynolds numbers investigated are in the range $5000 - 40000$. For low Re the membrane oscillates infrequently with small amplitudes, and acts similarly to a rigid splitter plate, by suppressing the vortex wake. By increasing Re to an order of 10000, the

membrane oscillates with a fairly constant frequency, however the membrane is not well coupled with the flow and exhibits a damping effect on the vortex street. As the Reynolds number increases further the amplitude in the oscillations increase, while the effective length of the membrane decreases. Furthermore, as the membrane wavelength shortens, the flow downstream of the cylinder begins to resemble the wake without a membrane being present. The amplitude of the wave propagating through the membrane reaches a maximum, whilst its frequency continues to increase linearly with Re. The membranes used are in the weight range $7 - 53$ grams, which is much lighter than an AIAUV. The observations made might not apply to bigger and heavier objects, and the vortex wake behavior might change drastically. The membrane is also more flexible than an AIAUV, and inducing an undulatory motion in a more rigid structure might require a larger bluff body or higher fluid velocities.

The behavior of a passive snake-like swimmer in the wake of bluff bodies was also studied computationally in Eldredge and Pisani (2008), and the results indicate that a steady-state distance to the bluff body can be achieved through leading-edge suction and upstream-oriented skin friction on the forebody of the swimmer. These observations were investigated in greater detail by locking the hinges between each body, which resulted in a straight swimmer similar to a fin. The swimmer achieved equilibrium with the stiff configuration as well suggesting that undulatory motion is not necessary to attain a forward thrust. However, due to the short simulation time in Eldredge and Pisani (2008), it is not possible to assess the stability of the vertical position of the snake-like structure, which oscillates with an increasing amplitude. This suggests that developing methods for stabilizing these oscillations might be necessary. Furthermore, the simulations studied are limited to $Re = 100$, and as seen in Allen and Smits (2001), the behavior of a swimmer changes with increasing Re. The size of the AIAUV and the operational environment will most likely result in Re of order 10000. Developing methods for achieving forward thrust by using the upstream-oriented skin friction might yield good results for achieving energy efficient propulsion. However, further investigation for higher Re is required before assessing if this is viable for the AIAUV.

Both Allen and Smits (2001) and Eldredge and Pisani (2008) present a study of how snake-like structures behave when placed in the wake of bluff bodies, however, the energy harvesting capabilities are only mentioned and not investigated in detail. Furthermore these structures are passive, which is a major difference from the AIAUV.

The energy harvesting capabilities of an articulated three-body swimmer were investigated computationally in Bernier et al. (2019). The bodies are given as separated elliptical shapes and they are connected through rotational dampers. The energy dissipated in the dampers is compared to the total energy needed to tow the cylinder and swimmer at stream velocity. Several different damping coefficients were studied, and an harvesting efficiency of 29.14% was achieved. The results indicate that there is an optimal damping coefficient which can be found. The lowest damping coefficient gave a harvesting efficiency of 0.54%, increasing the damping coefficient results in better harvesting efficiency until 29.14%. Increasing the damping coefficient past this decreases the harvesting efficiency, and the largest damping coefficient gives a harvesting efficiency of 5.26%. However, nine different damping coefficients are tested and only two of these are higher than the damping coefficient with the highest harvesting efficiency. Furthermore, changing other parameters, such as distance to the cylinder and body shapes, might yield better harvesting efficiency.

A computational study of efficient propulsion for articulated swimmers was performed in Bernier et al. (2018). A four-body swimmer is placed in the wake of a stationary cylinder and a moving cylinder, and compared to a swimmer in an uniform flow. The results show that the power consumed to stabilize the swimmer is 14% and 7% for the stationary and moving cylinder respectively. The study was performed with only one configuration for the swimmer, testing with different parameters might yield better efficiency. Furthermore, the methods used to track the cylinder only consider the distance and vorticity surrounding the cylinder. The efficiency might be improved if methods for tracking bluff bodies also considered the optimal path and configuration to generate energy while propagating towards the bluff body.

Both the studies Bernier et al. (2018) and Bernier et al. (2019) were performed at low $Re = 100$, and as mentioned earlier, this is very small compared to what can be expected for the AIAUV. Assessing the viability of these studies for larger swimmers in more turbulent environments requires more research.

2.2 Simulation models

A method for simulating the interaction between two-dimensional rigid bodies and a fluid flow is presented in Eldredge (2006a). The simulation is developed through the use of the vortex particle mesh method, where the fluid domain is divided into particles and the velocity field is found by evaluating the creation, diffusion and convection of vorticity in the particles. This simulation model is extended in Eldredge

(2006b) to allow the study of free swimming. This is done by exploiting the physical connection between vorticity and body motion. The motion of the body and the dynamics of the fluid are calculated simultaneously. While the actuation of the hinges between the bodies in the swimmer are predetermined, the changes in the position of the swimmer are not.

A simulation algorithm for a two-way coupling of an incompressible flow with single or multiple swimmers in the wake of bluff bodies is presented in Gazzola et al. (2011). The fluid domain is extended inside the solid body, and a penalization term is added to the governing Navier-Stokes equations. The algorithm handles deforming bodies and non-divergence free deformation in the velocity fields. The geometry of the swimmers is represented by a mollified characteristic function built upon a level set function to specify the interface between the boundary of the body and the fluid. However, this algorithm assumes that the kinematics of the swimmers are known a priori, and then the fluid-structure interaction (FSI) coupling is applied to the entire swimmer as a whole. Generally very few numerical works consider the internal dynamics of the swimmer.

This issue was addressed in Bernier et al. (2019), were the algorithm presented in Gazzola et al. (2011) is altered to include a multi-body system (MBS) solver to handle the hydrodynamic forces computed through the penalization term, and apply these to each individual body of the swimmer together with other internal forces inside the MBS. This allows for treatment of articulated systems with embedded actuation. The algorithm is verified through several well-documented simulation cases, and the results are reproduced with good accuracy.

2.3   Control system

For the past few years the path following and guidance algorithms for snake robots have been in focus. In Liljebäck et al. (2012) the Line-of-sight (LOS) guidance law is proven to κ-exponentially stabilize a ground snake robot to any desired path, assuming that the forward velocity is non-zero and positive. However, this does not apply for USRs where disturbances such as the ocean currents are present. This issue is addressed in Kohl et al. (2016) where the integral line-of-sight (ILOS) guidance law was proposed for USRs. The method is then proven to exponentially stabilize the heading of the USR and allows it to converge to a deisred straight path in the presence of constant irrotational currents. However, placing the USR downstream in the wake of a bluff body will result in disturbances that are rotational and varying

with time.

A articulated swimmer that tracks the wake of a moving cylinder is implemented and studied in Bernier et al. (2018). This is achieved by using the simulation method presented in Bernier et al. (2019), which is discussed in the previous section. The controller implemented is separated in three parts, a propulsion controller, a position controller and a steering controller. Forward propulsion is attained by the use of a sinusoidal gate, where kinematic tracking is achieved through a proportional controller. The distance to the cylinder is adjusted by using a PI controller to regulate the amplitude of the sinusoidal gate. To steer the snake robot in direction of the moving bluff body, two antennas are used to sense the vorticity on both sides of the swimmer. The difference between the sensed vorticities is then added to the sinusoidal gate as a turning term. The results indicate that the articulated swimmer does achieve tracking, but it does oscillate about the desired position with a large amplitude, and there is a significant phase offset in the vertical position. This is probably a result of the simple controller used for the kinematic tracking, proportional controllers are not robust enough for the disturbances present in a vortex street, and will result in substantial deviations from the desired values.

Chapter 3

Simulations and fluid dynamics

In this chapter a brief overview of the relevant fluid mechanics theory for the simulations in this thesis are presented.

The simulations in this thesis study the vortices that form in the wake of bluff bodies and how submerged bodies downstream interact with the wake of the bluff body. A bluff body is defined as a body that, as a result of its shape, has separated flow over a substantial part of its surface. Simulations which can capture the (FSI) between submerged swimmers and bluff body wakes are necessary. There are several different approaches to this problem. First, the Navier-Stokes equations are presented, before the vortex shedding phenomenon is discussed. Then, the approach taken by Gazzola et al. (2011) and Bernier et al. (2019) to maintain the boundary between solid and fluid, and the calculation of hydrodynamic efforts on submerged bodies is presented. Finally, the finite element method FEM is briefly discussed.

3.1 The Navier-Stokes equations

The Navier-Stokes equation governs the motion of viscous fluids and is often used to model the fluid flow through pipes and around objects. The compressible Navier-Stokes equation as presented in Newman (2018) is given by

$$\rho \left(\frac{\partial \boldsymbol{u}}{\partial t} + \boldsymbol{u} \cdot \nabla \boldsymbol{u} \right) = -\nabla p + \nabla \cdot (\mu (\nabla \boldsymbol{u} + (\nabla \boldsymbol{u})^T) - \frac{2}{3} \mu (\nabla \cdot \boldsymbol{u}) \boldsymbol{I}) + \boldsymbol{F}, \qquad (3.1)$$

where $\boldsymbol{u}$ is the fluid velocity, p is the fluid pressure, ρ is the fluid density, μ is the fluid dynamic viscosity and $\boldsymbol{F}$ are the external forces applied to the fluid. The identity matrix is given as I. Furthermore, the Navier-Stokes equation is always solved

together with the continuity equation

$$\frac{\partial \rho}{\partial t} + \nabla \cdot (\rho \boldsymbol{u}) = 0 \tag{3.2}$$

The Navier-Stokes equation can be further simplified for incompressible fluids, which is usually done for Mach numbers under 0.3. Where the mach number is defined as the ratio of fluid flow past a boundary to the speed of sound in the medium. Because low Mach numbers are generally found in liquids, the simplified Navier-Stokes equation gives a good approximation in this case. The incompressible Navier-Stokes equation is given by

$$\rho \left(\frac{\partial \boldsymbol{u}}{\partial t} + \boldsymbol{u} \cdot \nabla \boldsymbol{u} \right) = -\nabla p + \mu \nabla^2 \boldsymbol{u} + \boldsymbol{F}, \tag{3.3}$$

while the continuity equation simplifies to

$$\nabla \cdot \boldsymbol{u} = 0. \tag{3.4}$$

Furthermore, by taking the curl of the Navier-stokes equation, the vorticity equation can be derived, which describes the evolution of vorticity ω of a particle in a fluid. The transformation from velocity to vorticity is given as the curl of the velocity

$$\boldsymbol{\omega} = \nabla \times \boldsymbol{u}. \tag{3.5}$$

Inserting this into eq. (3.3), yields the vorticity equation

$$\frac{D\boldsymbol{\omega}}{Dt} = (\boldsymbol{\omega} \cdot \nabla)\boldsymbol{u} + \mu \nabla^2 \boldsymbol{\omega}, \tag{3.6}$$

where $\dfrac{D}{Dt}$ denotes the material derivative.

3.2   Kàrmàn vortex street

The theory presented in this section is based on Sumer et al. (2006), and further elaboration of the fluid dynamics surrounding cylinders can be found there.

Vortex shedding is a phenomenon that occurs when a fluid flows past a bluff body at certain Reynolds numbers and mass ratios. The flow creates alternating vortices that shed off of the bluff body forming a Von Kàrmàn vortex street as seen in fig. 3.1 below.
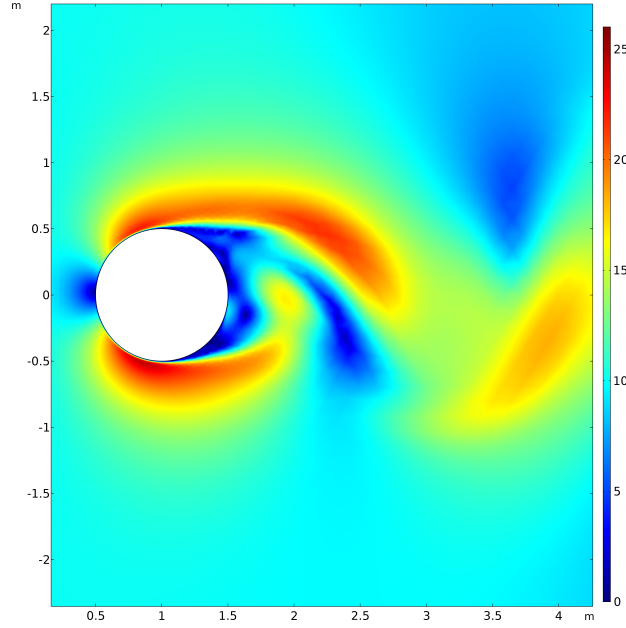
Figure 3.1: Von Kàrmàn vortex street behind a cylinder

Vortex shedding is characterized by a nondimensional parameter known as the Strouhal number defined as

$$S_t = \frac{f_v D}{U_\infty},$$ (3.7)

where f_v is the vortex shedding frequency, U_∞ is the free stream velocity and D is the diameter of the cylinder. Furthermore, the shape of the vortices shed and the size of the Kàrmàn vortex street is dependent on the shape and surface of the bluff body, but in this thesis the study is limited to cylinders.

The non-dimensional quantities describing the flow around a cylinder depend on the cylinder Reynolds number given by

$$Re = \frac{D U_\infty}{\nu},$$ (3.8)

where ν is the kinematic viscosity. Flow separation does not occur for very small Reynolds numbers $Re < 5$, hence there are very small disturbances in the flow. For the range of Reynolds numbers $5 < Re < 40$, a fixed pair of vortices form a wake behind the cylinder. For higher Reynolds numbers, the wake destabilizes, eventually resulting in vortex shedding with a frequency given by eq. (3.7). When the Reynolds number is in the range $40 < Re < 200$, the Kàrmàn vortex street is laminar, which means it is essentially two dimensional because it does not vary along the height of

the cylinder. Increasing the Reynolds number further results in a gradual transition to a turbulent wake, and the two dimensional property of the Kàrman vortex street is lost. The vortices are then shed in cells along the height of the cylinder and the vortex street becomes three-dimensional.

In this thesis it is assumed that the vortex shedding is laminar, therefore two-dimensional. The evolution of the Kàrmàn vortex street with increasing Reynolds numbers past $Re = 200$ will not be considered.

3.3   Fluid-structure interaction

The theory presented in this section is based on the simulator developed in Gazzola et al. (2011) and Coquerelle and Cottet (2008), and later extended by Bernier et al. (2018).

3.3.1   Brinkman penalization and the no-slip condition

To simulate flows around solid objects several immersed boundary methods have been developed. The Brinkman penalization method was first proposed for incompressible viscous flows. The no-slip conditions at the surface of the submerged object are enforced by adding a penalty term to the Navier-Stokes equation. The immersed objects geometry is represented by a mollified characteristic function χ_s, given by

$$\chi_s = \begin{cases} 0 & \text{if } d < -\eta \\ \dfrac{1}{2}\left(1 + \dfrac{d}{\eta} + \dfrac{1}{\pi}\sin\pi\dfrac{d}{\eta}\right) & \text{if } |d| \leq \eta \\ 1 & \text{if } d > \eta, \end{cases} \tag{3.9}$$

where d is the distance to the surface of the body and η is the mollification length. The fluid domain is extended to include the rigid bodies, combining the solid and fluid domains to one continuous domain. The Navier-Stokes equations are then extended with a term that drives the fluid velocity $\boldsymbol{u}$ inside the solid region to a prescribed rigid body velocity $\boldsymbol{u}_s$. This gives the modified Navier-Stokes equation

$$\rho\left(\frac{\partial \boldsymbol{u}}{\partial t} + \boldsymbol{u}\cdot\nabla\boldsymbol{u}\right) = -\nabla p + \mu\nabla^2\boldsymbol{u} + \lambda\chi_s(\boldsymbol{u}_s - \boldsymbol{u}) + \boldsymbol{F}, \tag{3.10}$$

where λ is the penalization factor where larger values enforce the no-slip condition more strictly, but also make the system dynamics stiffer. The Navier-stokes equations can also be written in the vorticity formulation eq. (3.6) with the added penalization

term

$$\frac{D\boldsymbol{\omega}}{Dt} = (\boldsymbol{\omega} \cdot \nabla)\boldsymbol{u} + \mu\nabla^2\boldsymbol{\omega} + \lambda\nabla \times (\chi_s(\boldsymbol{u}_s - \boldsymbol{u})). \tag{3.11}$$

Where the Baroclinic generation of vorticity is left out because of the assumption that the fluid and solid regions are uniform across the respective bodies.

3.3.2 Forces and moments on submerged rigid bodies

The hydrodynamic forces exerted on the submerged objects have to be calculated. In Bernier et al. (2019) the forces and moments exerted by the vortices and fluid flow are derived by integrating over the boundary between the fluid and volume Ω_j

$$F_{\text{hyd}_j} = \int_{\delta\Omega_j} \sigma \cdot \boldsymbol{n}dS, \tag{3.12}$$

$$M_{\text{hyd}_j} = \int_{\delta\Omega_j} \boldsymbol{x} \times (\sigma \cdot \boldsymbol{n})dS. \tag{3.13}$$

Where the volume Ω_i is the area of each link, σ is the Cauchy stress tensor and $\delta\Omega_i$ is the boundary between each link and the fluid. By using Green's Theorem and the conservative form of the Navier-Stokes equations, given by

$$\rho_f \frac{D\boldsymbol{u}}{Dt} = \nabla \cdot \sigma + \rho_f \lambda(\boldsymbol{u}_s - \boldsymbol{u}) \tag{3.14}$$

the following expressions are derived in Bernier et al. (2019)

$$F_{\text{hyd}_j} = \frac{d}{dt} \int_{\Omega_j} (\rho_f \boldsymbol{u})dV + \int_{\Omega_j} \rho_f \lambda(\boldsymbol{u} - \boldsymbol{u}_s)dV, \tag{3.15}$$

$$M_{\text{hyd}_j} = \frac{d}{dt} \int_{\Omega_j} \boldsymbol{x} \times (\rho_f \boldsymbol{u})dV + \int_{\Omega_j} \boldsymbol{x} \times (\rho_f \lambda(\boldsymbol{u} - \boldsymbol{u}_s))dV. \tag{3.16}$$

In this thesis it is assumed that the hydrodynamic forces and moments are extracted by using the approach presented in this section. However, other computational fluid dynamics (CFD) solvers may solve this problem with a different approach.

3.4 Discretization method

The mathematical equations that represent the simulation have to be approximated through the use of a discretization method, which is a method of approximating the differential equations with a set of algebraic equations. The most common

discretization methods are the finite difference method (FEM), the finite volume method (FVM) and the finite element method (FEM). In COMSOL Multiphysics both the FVM and the FEM can be used. For the simulations developed in this thesis the FEM is selected therefore it will be presented in this section. The theory presented in this section is based on Pepper and Heinrich (2017) and Ferziger and Perić (1999).

The finite element method is a numerical technique that can be used to find approximate solutions of differential equations, and is typically used for problems in hydrodynamics, aerodynamics and structural dynamics. The FEM reduces problems defined on a domain to finding solutions in a finite number of points by dividing the domain into smaller geometrical regions, for two-dimensional simulations triangles and squares are often used. This creates a mesh over the geometrical domain, and adjusting the density of the mesh allows for more accurate approximations at the cost of computational time. The usual approach is to begin with a coarse mesh, and increase the density slowly until the desired trade off between accuracy and computational time has been reached.

The FVM and FEM are similar, but a distinguishing factor of the FEM is that the equations are multiplied with a weight function, before they are integrated over the entire domain. The simplest form of the FEM approximates solutions by linear shape functions within each element in a way that guarantees continuity of the solution across element boundaries. This function is constructed from its values at the corners of each element, and the weight function is usually of the same form.

The size of elements in the mesh might also vary. To reduce computational time, while ensuring accurate solutions, more elements can be placed in the regions where functions are expected to change more rapidly. For example to study the Kàrmàn vortex street behind a cylinder, the majority of changes are happening at the boundary between the cylinder and the fluid, hence smaller elements should be used close to the cylinder. As the distance to the cylinder increases, there are less changes in the fluid flow, hence the size of each element can be increased without losing much accuracy.

The process of finding a suitable mesh for the physical domain might require several iterations, and small changes to the cells of the mesh might affect the results severely. In this thesis the simulations studied are two-dimensional, hence only two-dimensional meshing will be considered.

The mathematics behind the FEM are handled by COMSOL Multiphyics, and will therefore not be stated in this thesis, for further reading the reader is referred to Pepper and Heinrich (2017) or the COMSOL Multipysics Reference Manual, COMSOL

(2019).

Chapter 4

Simulation models

In this chapter the mathematical models describing the equations of motion of four passive systems are presented. The first model describes a double pendulum connected to a cylinder by a spring and damper. The second model describes a quadratic box connected to a cylinder and the ground with two springs and dampers. The third model describes a three link swimmer, where the first link is constrained to not move or rotate. The fourth model is a three link swimmer, where the links are separated, allowing fluid to flow betwwen the links. The links are connected by linear springs, and the first link is connected to a cylinder via a linear spring.

These four simulation models were developed and studied in order to better understand the energy harvesting capabilities of an articulated intervention autonomous underwater vehicle (AIAUV), and how a simulation model with FSI between the swimmer and fluid can be developed.

4.1 Deriving the equations of motion

In this section the theory for deriving the Euler-Lagrange equations of motion are presented. All of the systems are composed of links connected by linear and rotational springs. The kinetic and potential energies of the systems can therefore be expressed in a modular fashion.

4.1.1 Reference frames

In order to describe the dynamics of the systems, two coordinate systems are needed, the inertial frame $[i]$ and the body frame $[b]$.

The inertial frame is usually defined as the tangent plane on the surface of the

earth, and the origin can be placed arbitrarily. In this work, the unit vector $\boldsymbol{k}^i$ is chosen to point upwards

The body frame is attached to the submerged object and the origin is placed at a arbitrary point on the body. The axis $\boldsymbol{i}^b$ usually points in the forward direction, while $\boldsymbol{j}^b$ points to the left. The axis $\boldsymbol{k}^b$ points upwards.

4.1.2   Spring and damper force, energy and moment

The potential energy of the system is the energy stored in the linear and rotational springs, which can be written as

$$V(\varphi) \triangleq \sum_{i=1}^{N} K_{l_i} r_i^2 + \sum_{j=1}^{M} K_{r_j} \phi_j^2. \tag{4.1}$$

Where r_i is the displacement from nominal position of the linear spring, and N is the number of linear springs in the system. The relative rotation between the links is given by ϕ_j and the number of rotational springs is given by M. The linear and rotational spring stiffness coefficients are given by K_l and K_r. The generalized coordinates of the system are given by φ.

The linear damping forces exerted on the system are given by the time derivative of the displacement r_i, this can be defined as

$$\boldsymbol{F}_{\text{damper}} \triangleq -\sum_{i=1}^{N} B_{l_i} \dot{r}_i \, \boldsymbol{u}, \tag{4.2}$$

where $\boldsymbol{u} = [\cos \alpha, \ \sin \alpha]^T$ is the unit velocity vector relating the force components to the inertial frame, and B_l is the damping coefficient. The rotational dampers induce a moment in the system given by

$$\boldsymbol{M}_{\text{damper}} \triangleq -\sum_{j=1}^{M} B_{r_j} \dot{\phi}_j, \tag{4.3}$$

where the rotational damping coefficient is given by B_r.

The energy dissipated by the damper can be derived by integrating the power of the damper, which gives the following equation for the rotational dampers

$$E_{d_i} = \int_{t_0}^{t} B_{r_i} \dot{\phi}_i(\tau)^2 d\tau. \tag{4.4}$$

4.1.3 Kinetic energy

The rigid body kinetic energy of the systems is defined as

$$T(\varphi, \dot{\varphi}) \triangleq \sum_{j=1}^{N} \frac{1}{2} \boldsymbol{v}_j^T M_j \boldsymbol{v}_j, \tag{4.5}$$

where v is the body frame velocity and M is the rigid body mass matrix of the submerged object. The body frame velocity can be related to the generalized coordinates by the following equation

$$\boldsymbol{v}_i \triangleq \boldsymbol{J}_i(\varphi)\dot{\varphi}, \tag{4.6}$$

where $\boldsymbol{J}(\varphi)$ is the Jacobian of the submerged object. By following the approach presented in Fossen (2011) the following rigid body matrix is defined

$$\boldsymbol{M}_{RB} \triangleq \begin{bmatrix} m & 0 & -my_g \\ 0 & m & mx_g \\ -my_g & mx_g & I \end{bmatrix}, \tag{4.7}$$

where $[x_g, \ y_g]^T$ is the vector from the origin of the body frame to the centre of gravity (CG), and I is the moment of inertia about the unit z-axis.

4.1.4 Forward kinematics

The forward kinematics of a submerged object given in the inertial frame is defined as $\boldsymbol{P}_i$, and this can be differentiated with respect to time to find the velocity of the submerged object $\boldsymbol{V}_i = \dot{\boldsymbol{p}}_i$. The body frame velocity $\boldsymbol{v}_i$ can be related to the inertial body velocity by

$$\boldsymbol{v}_i \triangleq \boldsymbol{R}(\beta_i)^T V_i, \tag{4.8}$$

where the rotational matrix R is given as a rotation about the $\boldsymbol{k}^i$ unit vector

$$\boldsymbol{R}(\beta) = \begin{bmatrix} \cos \beta_i & -\sin \beta_i & 0 \\ \sin \beta_i & \cos \beta_i & 0 \\ 0 & 0 & 1 \end{bmatrix}. \tag{4.9}$$

4.1.5   Lagrange's equation of motion

Lagrange's equation of motion are derived by using the Lagrangian:

$$\mathcal{L}(\varphi, \dot{\varphi}) = T(\varphi, \dot{\varphi}) - V(\varphi). \qquad (4.10)$$

The equations describing the dynamics of the system are then given by the Euler-Lagrange equation

$$\frac{d}{dt}\frac{\partial \mathcal{L}}{\partial \dot{\varphi}} - \frac{\partial \mathcal{L}}{\partial \varphi} = f(\varphi), \qquad (4.11)$$

where $f(\varphi)$ are the generalized forces acting on the system. For the systems presented in this thesis, the generalized forces are the damping forces and hydrodynamic forces. The damping forces can be written as a Rayleigh dissipation function

$$D(\varphi, \dot{\varphi}) = \frac{1}{2}\dot{\varphi}^T \mathbf{B}(\varphi)\dot{\varphi}. \qquad (4.12)$$

Furthermore the hydrodynamic forces and moments can be calculated as presented in section 3.3.2, the reader is referred to COMSOL (2019) for more details. The following assumption is made

Assumption 4.1 *The calculation of hydrodynamic forces and moments is handled by the CFD software.*

For the three models presented in this chapter, the calculations are performed through COMSOL Multiphysics.

The rewritten Euler-Lagrange equations are given by

$$\frac{d}{dt}\frac{\partial \mathcal{L}}{\partial \dot{\varphi}} - \frac{\partial \mathcal{L}}{\partial \varphi} = -\frac{\partial D}{\partial \dot{\varphi}} + \xi(\varphi), \qquad (4.13)$$

where the hydrodynamic forces and moments are given by $\xi(\varphi)$.

4.2   Model for double pendulum with spring

The model presented in this section describes a double pendulum (DP) connected to a cylinder with a spring and damper. First an overview of the system is presented, and then The equations of motion are derived using the Euler-Lagrange equations.

4.2.1 Model overview

The system is illustrated in fig. 4.1. In order for the passive DP to hold a steady distance to the cylinder without being dragged by the flow, a spring and damper are connected between the first link and the cylinder. The spring and damper are both connected to the centre of the cylinder and to the front of the first link.
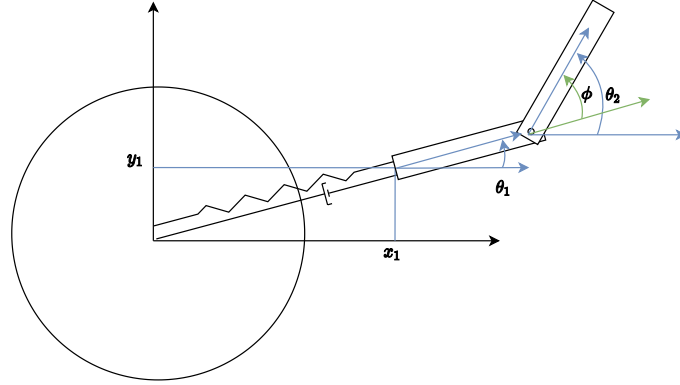

Figure 4.1: Overview of double pendulum with spring and damper

Furthermore the spring and damper can rotate about the centre of the cylinder. The following assumption is made,

Assumption 4.2 *The spring and damper are massless and do not interact with the fluid directly.*

A rotational spring and damper are also added to the joint between the links in the double pendulum. The distance from the centre of the cylinder to the first link is given by x_1 and y_1, and the rotation of each joint is given by θ_1 and θ_2. The global coordinates are then

$$\vartheta_1 = \begin{bmatrix} x_1, & y_1, & \theta_1 \end{bmatrix}^T, \tag{4.14}$$

$$\vartheta_2 = \begin{bmatrix} x_2, & y_2, & \theta_2 \end{bmatrix}^T. \tag{4.15}$$

The relative joint angle is also defined

$$\phi_1 = \theta_2 - \theta_1. \tag{4.16}$$

The energy dissipated in the rotational damper between the links will be considered when assessing the energy harvesting capabilities of the system.

4.2.2   Equations of motion

To derive the equations of motion for the system, first the generalized coordinates for the system are chosen according to the illustration in fig. 4.1 as

$$\varphi = \begin{bmatrix} x_1, \ y_1, \ \theta_1, \ \phi_1 \end{bmatrix}^T. \tag{4.17}$$

First the forward kinematics of the DP are derived. The position of the first and second links are

$$P_1 = \begin{bmatrix} x_1, \ y_1, \ \theta_1 \end{bmatrix}^T, \tag{4.18}$$

$$P_2 = \begin{bmatrix} x_1 + l_1 \cos \theta_1, \ y_1 + l_1 \sin \theta_1, \ \theta_1 + \phi_1 \end{bmatrix}^T. \tag{4.19}$$

Where l_1 and l_2 are the lengths of the first and second link. Furthermore, the velocity of each link in the inertial frame can be obtained by calculating the time derivative of eqs. (4.18)–(4.19)

$$V_1 = \begin{bmatrix} \dot{x}_1, \ \dot{y}_1, \ \dot{\theta}_1 \end{bmatrix}^T, \tag{4.20}$$

$$V_2 = \begin{bmatrix} \dot{x}_1 - l_1 \dot{\theta}_1 \sin \theta_1, \ \dot{y}_1 + l_1 \dot{\theta}_1 \cos \theta_1, \ \dot{\theta}_1 + \dot{\phi}_1 \end{bmatrix}^T. \tag{4.21}$$

By using eq. (4.8) and eq. (4.6), and the angles $\beta_1 = \theta_1$ and $\beta_2 = \theta_1 + \phi_1$, the Jacobians for the first and second links can be derived

$$J_1(\varphi) = \begin{bmatrix} \cos \theta_1 & \sin \theta_1 & 0 & 0 \\ -\sin \theta_1 & \cos \theta_1 & 0 & 0 \\ 0 & 0 & 1 & 0 \end{bmatrix}, \tag{4.22}$$

$$J_2(\varphi) = \begin{bmatrix} \cos \theta_1 + \phi_1 & \sin \theta_1 + \phi_1 & l_1 \sin \theta_1 & 0 \\ -\sin \theta_1 + \phi_1 & \cos \theta_1 + \phi_1 & l_1 \cos \theta_1 & 0 \\ 0 & 0 & 1 & 1 \end{bmatrix}. \tag{4.23}$$

The rigid body kinetic energy of the system is given by eq. (4.5), yielding

$$T(\varphi, \dot{\varphi}) = \frac{1}{2} v_1^T M_1 v_1 + \frac{1}{2} v_2^T M_2 v_2. \tag{4.24}$$

Where $\boldsymbol{M}_1$ and $\boldsymbol{M}_2$ are the rigid body mass matrices for each link, given by

$$\boldsymbol{M}_1 = \begin{bmatrix} m_1 & 0 & 0 \\ 0 & m_1 & m_1\frac{1}{2}l_1 \\ 0 & m_1\frac{1}{2}l_1 & I \end{bmatrix}, \tag{4.25}$$

$$\boldsymbol{M}_2 = \begin{bmatrix} m_2 & 0 & 0 \\ 0 & m_2 & m_2\frac{1}{2}l_2 \\ 0 & m_2\frac{1}{2}l_2 & I \end{bmatrix}. \tag{4.26}$$

The potential energy of the system can be found by using eq. (4.1). The model has one linear spring and damper, and one rotational spring and damper, which gives

$$V(\varphi) = \frac{1}{2}K_{l_1}(x_1^2 + y_1^2) + \frac{1}{2}K_{r_1}\phi_1^2, \tag{4.27}$$

when assuming that the linear spring has a resting position at $x = y = 0$. The damping forces can be calculated by using eq. (4.1) and the angle

$$\alpha = \arctan\left(\frac{y_1}{x_1}\right), \tag{4.28}$$

which gives

$$\boldsymbol{F}_{d_1} = B_{d_1}\frac{x_1\dot{x}_1 + y_1\dot{y}_1}{\sqrt{x_1^2 + y_1^2}}\begin{bmatrix} \dfrac{x_1}{\sqrt{x_1^2 + y_1^2}} \\ \dfrac{y_1}{\sqrt{x_1^2 + y_1^2}} \end{bmatrix}. \tag{4.29}$$

The Rayleigh dissipation function eq. (4.12) for the system is derived, where $B(\varphi)$ is given by

$$\boldsymbol{B}(\varphi) = \begin{bmatrix} B_{l_1}\dfrac{x_1^2}{x_1^2 + y_1^2} & B_{l_1}\dfrac{x_1 y_1}{x_1^2 + y_1^2} & 0 & 0 \\ B_{l_1}\dfrac{x_1 y_1}{x_1^2 + y_1^2} & B_{l_1}\dfrac{y_1^2}{x_1^2 + y_1^2} & 0 & 0 \\ 0 & 0 & 0 & 0 \\ 0 & 0 & 0 & B_{r_1} \end{bmatrix}. \tag{4.30}$$

The Euler-Lagrange equations of motion for the system as given in eq. (4.13) are calculated. After performing some simplifications with MATLAB the following

equations of motion are found

$$0 = (m_1 + m_2)\ddot{x}_1 - \frac{1}{2}l_2 m_2 \sin(\phi_1 + \theta_1)(\ddot{\phi}_1 + \ddot{\theta}_1) - \frac{1}{2}l_2 m_2 \cos(\phi_1 + \theta_1)(\dot{\phi}_1 + \dot{\theta}_1)^2$$

$$- l_1 m_2 \ddot{\theta}_1 \sin\phi_1 - l_1 m_2 \dot{\phi}_1 \dot{\theta}_1 \cos\theta_1 - \frac{1}{2}l_1 m_1 \ddot{\theta}_1 \sin\theta_1 - \frac{1}{2}l_1 m_1 \dot{\theta}_1^2 \cos\theta_1 - K_{l_1} x_1$$

$$+ B_{l_1}\frac{x_1(x_1\dot{x}_1 + y_1\dot{y}_1)}{x_1^2 + y_1^2} - \xi_x$$

$$(4.31)$$

$$0 = (m_1 + m_2)\ddot{y}_1 + \frac{1}{2}l_2 m_2 \cos(\phi_1 + \theta_1)(\ddot{\phi}_1 + \ddot{\theta}_1) - \frac{1}{2}l_2 m_2 \sin(\phi_1 + \theta_1)(\dot{\phi}_1 + \dot{\theta}_1)^2$$

$$+ l_1 m_2 \ddot{\theta}_1 \cos(\phi_1) - l_1 m_2 \dot{\theta}_1 \dot{\phi} - 1 \sin\phi_1 + \frac{1}{2}l_1 m_1 \ddot{\theta}_1 \cos\theta_1 - \frac{1}{2}l_1 m_1 \dot{\theta}_1^2 \sin\theta_1$$

$$+ K_{l_1} y_1 + B_{l_1}\frac{y_1(x_1\dot{x}_1 + y_1\dot{y}_1)}{x_1^2 + y_1^2} - \xi_y$$

$$(4.32)$$

$$0 = I\ddot{\phi}_1 + I\ddot{\theta}_1 + \frac{1}{2}l_2 m_2 \ddot{y}_1 \cos(\phi_1 + \theta_1) - \frac{1}{2}l_2 m_2 \dot{y}_1 \sin(\phi_1 + \theta_1)(\dot{\phi}_1 + \dot{\theta}_1)$$

$$- \frac{1}{2}l_2 m_2 \ddot{x}_1 \sin(\phi_1 + \theta_1) - \frac{1}{2}l_2 m_2 \dot{x}_1 \cos(\phi_1 + \theta_1)(\dot{\phi}_1 + \dot{\theta}_1) + \frac{1}{2}l_1 l_2 m_2 \ddot{\theta}_1 \cos\theta_1$$

$$- \frac{1}{2}l_1 l_2 m_2 \dot{\theta}_1^2 \sin\theta_1 - K_{r_1}\dot{\phi}_1 + l_1 m_2 \dot{\theta}_1 \dot{y}_1 \sin\phi_1 + \frac{1}{2}l_2 m_2 \dot{\phi}_1 \dot{x}_1 \cos(\phi_1 + \theta_1)$$

$$+ \frac{1}{2}l_2 m_2 \dot{\theta}_1 \dot{x}_1 \cos(\phi_1 + \theta_1) + \frac{1}{2}l_2 m_2 \dot{\phi}_1 \dot{y}_1 \sin(\phi_1 + \theta_1) + \frac{1}{2}l_2 m_2 \dot{\theta}_1 \dot{y}_1 \sin(\phi_1 + \theta_1)$$

$$+ l_1 m_2 \dot{\theta}_1 \dot{x}_1 \cos\phi_1 + B_{r_1}\dot{\phi}_1 - \xi_{\phi_1}$$

$$(4.33)$$

$$0 = I\ddot{\phi}_1 + 2I\ddot{\theta}_1 + l_1^2 m_2 \ddot{\theta}_1 + \frac{1}{2}l_2 m_2 \ddot{y}_1 \cos(\phi_1 + \theta_1) - \frac{1}{2}l_2 m_2 \dot{y}_1 \sin(\phi + \theta)(\dot{\phi}_1 + \dot{\theta}_1)$$

$$- \frac{1}{2}l_2 m_2 \ddot{x}_1 \sin(\phi_1 + \theta_1) - \frac{1}{2}l_2 m_2 \dot{x}_1 \cos(\phi_1 + \theta_1)(\dot{\phi}_1 + \dot{\theta}_1) + l_1 m_2 \ddot{y}_1 \cos\theta_1$$

$$- l_1 m_2 \dot{y}_1 \dot{\phi}_1 \sin\phi_1 + \frac{1}{2}l_1 m_1 \ddot{y}_1 \cos\theta_1 - \frac{1}{2}l_1 m_1 \dot{y}_1 \dot{\theta} \cos\theta_1 - l_1 m_2 \ddot{x}_1 \sin\phi_1$$

$$- l_1 m_2 \dot{x}_1 \dot{\phi}_1 \cos\phi - \frac{1}{2}l_1 m_1 \ddot{x}_1 \sin\theta_1 - \frac{1}{2}l_1 m_1 \dot{x}_1 \dot{\theta}_1 \cos\theta_1 + \frac{1}{2}l_1 l_2 m_2 \ddot{\phi}_1 \cos\theta_1$$

$$- \frac{1}{2}l_1 l_2 m_2 \dot{\phi}_1 \dot{\theta}_1 \sin\theta_1 + l_1 l_2 m_2 \ddot{\theta}_1 \cos\theta_1 - l_1 l_2 m_2 \dot{\theta}_1^2 \sin\theta_1 + \frac{1}{2}l_1 m_1 \dot{\theta}_1 \dot{y}_1 \sin\theta_1$$

$$+ \frac{1}{2}l_1 l_2 m_2 \dot{\theta}_1^2 \sin\theta_1 + \frac{1}{2}l_2 m_2 \dot{\phi}_1 \dot{x}_1 \cos(\phi_1 + \theta_1) + \frac{1}{2}l_2 m_2 \dot{\theta}_1 \dot{x}_1 \cos(\phi_1 + \theta_1)$$

$$+ \frac{1}{2}l_2 m_2 \dot{\phi}_1 \dot{y}_1 \sin(\phi_1 + \theta_1) + \frac{1}{2}l_2 m_2 \dot{\theta}_1 \dot{y}_1 \sin(\phi_1 + \theta_1) + \frac{1}{2}l_1 m_1 \dot{\theta}_1 \dot{x}_1 \cos\theta_1$$

$$+ \frac{1}{2}l_1 l_2 m_2 \dot{\phi}_1 \dot{\theta}_1 \sin\theta - \xi_{\theta_1}$$

$$(4.34)$$

4.3 Model for block with two springs and dampers

The model presented in the section describes a square block suspended by one horizontal and one vertical spring and damper, which will be denoted as BSD. First an overview is presented, then the equations of motion are derived.

4.3.1 Model overview

The system is illustrated in fig. 4.2. The model has simpler dynamics than the DP in section 4.2, which reduces the simulation time and allows for a less time consuming analysis when parameters are altered in the simulation environment.

The BSD is connected to the cylinder through a spring and damper to constrain the horizontal motion. The vortices shed from the cylinder induce a vertical motion in the block, to harvest this energy a vertical spring and damper is connected between the block and the lower wall. Both the horizontal and vertical springs and dampers are connected to the middle of the block.
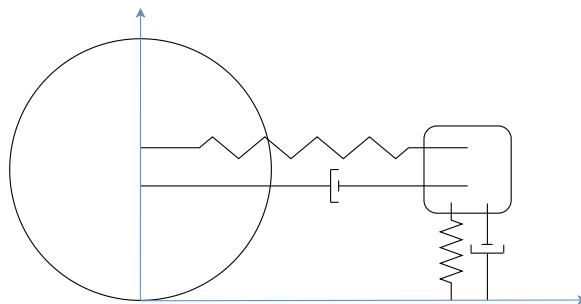

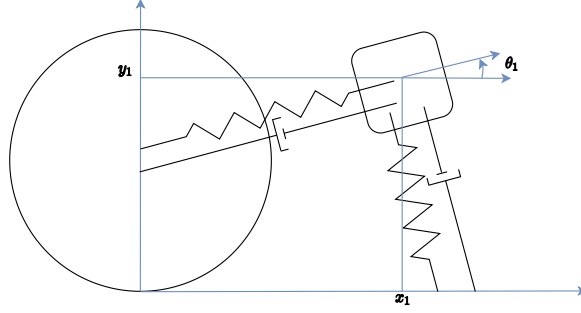**Figure 4.2:** Overview of block with two springs and dampers

Figure 4.3: Global coordinates of block with springs and dampers

The springs and dampers can rotate about the connection points at the lower wall and cylinder, but not about the block, as is illustrated in fig. 4.3. For this model, assumption 4.2 still holds. The distance from the centre of the cylinder to the centre of the block is given by x_1 and y_1, furthermore the rotation of the block is given by θ_1. The global coordinates are then given by

$$\boldsymbol{\vartheta} = \left[x_1, y_1, \theta_1 \right]^T .$$ (4.35)

The energy dissipated in the vertical damper will be considered when assessing the energy harvesting capabilities of the system.

4.3.2   Spring and damper forces and potential energy

The forces exerted by the springs are calculated using a similar approach to section 4.2.2, the force exerted by the horizontal spring is

$$\boldsymbol{F}_{s_H} = K_{s_H}(r_0 - \sqrt{x_1^2 + (r_1 - y_1)^2}) \begin{bmatrix} \dfrac{x_1}{\sqrt{x_1^2 + (r_1 - y_1)^2}} \\ \dfrac{r_1 - y_1}{\sqrt{x_1^2 + (r_1 - y_1)^2}} \end{bmatrix},$$ (4.36)

and for the vertical spring

$$\boldsymbol{F}_{s_V} = K_{s_V}(r_1 - \sqrt{(r_0 - x_1)^2 + y_1^2}) \begin{bmatrix} \dfrac{y_1}{\sqrt{(r_0 - x_1)^2 + y_1^2}} \\ \dfrac{r_0 - x_1}{\sqrt{(r_0 - x_1)^2 + y_1^2}} \end{bmatrix}.$$ (4.37)

Where r_0 and r_1 are the resting configurations of the horizontal and vertical springs respectively. The resting configuration as shown in fig. 4.2. Furthermore the damping forces are found to be

$$F_{d_H} = B_{d_H} \frac{(r_1 - y_1)(-\dot{y}_1) + x_1 \dot{x}_1}{\sqrt{x_1^2 + (r_1 - y_1)^2}} \begin{bmatrix} \dfrac{x_1}{\sqrt{x_1^2 + (r_1 - y_1)^2}} \\ \dfrac{r_1 - y_1}{\sqrt{x_1^2 + (r_1 - y_1)^2}} \end{bmatrix}, \tag{4.38}$$

$$F_{d_V} = B_{d_V} \frac{y_1 \dot{y}_1 + (r_0 - x_1)(-\dot{x}_1)}{\sqrt{(r_0 - x_1)^2 + y_1^2}} \begin{bmatrix} \dfrac{y_1}{\sqrt{(r_0 - x_1)^2 + y_1^2}} \\ \dfrac{r_0 - x_1}{\sqrt{(r_0 - x_1)^2 + y_1^2}} \end{bmatrix}. \tag{4.39}$$

The potential energy of the springs is given by

$$V(\varphi) = \frac{1}{2} K_{s_H}(x_1^2 + (r_1 - y_1)^2) + \frac{1}{2} K_{s_V}((r_0 - x_1)^2 + y_1^2). \tag{4.40}$$

4.3.3 Equations of motion

The forward kinematics are the same as for the first link in the DP presented in section 4.2.2. As shown in fig. 4.3 the generalized coordinates are chosen to be

$$\varphi = \begin{bmatrix} x_1, & y_1, & \theta_1 \end{bmatrix}^T. \tag{4.41}$$

The equations of motion are derived by following the approach presented in section 4.2.2. The Jacobian is the same as for the first link in the DP, given by eq. (4.22). The rigid body mass is different due to the origin being in the centre of mass, and is given by

$$M_1 = \begin{bmatrix} m & 0 & 0 \\ 0 & m & 0 \\ 0 & 0 & I \end{bmatrix}. \tag{4.42}$$

Furthermore the damping is described by eq. (4.12), where $B(\varphi)$ is given by

$$B(\varphi) = \begin{bmatrix} d_{11} & d_{12} & 0 \\ d_{21} & d_{22} & 0 \\ 0 & 0 & 0 \end{bmatrix}, \tag{4.43}$$

and the coefficients of the matrix are given by

$$d_{11} = \frac{B_{d_H} x_1^2}{x_1^2 + (r_1 - y_1)^2} - \frac{B_{d_V}(r_0 - x_1)y_1}{(r_0 - x_1)^2 + y_1^2}, \tag{4.44}$$

$$d_{12} = \frac{B_{d_V} y_1^2}{(r_0 - x_1)^2 + y_1^2} - \frac{B_{d_H}(r_1 - y_1)x_1}{x_1^2 + (r_1 - y_1)^2}, \tag{4.45}$$

$$d_{21} = \frac{B_{d_H}(r_1 - y_1)x_1}{x_1^2 + (r_1 - y_1)^2} - \frac{B_{d_V}(r_0 - x_1)^2}{(r_0 - x_1)^2 + y_1^2}, \tag{4.46}$$

and

$$d_{22} = \frac{B_{d_V}(r_0 - x_1)y_1}{(r_0 - x_1)^2 + y_1^2} - \frac{B_{d_H}(r_1 - y_1)^2}{x_1^2 + (r_1 - y_1)^2}. \tag{4.47}$$

The equations of motion are now derived by using the Euler-Lagrange equations given in eq. (4.13). After performing the calculations and simplifying, the following equations of motion are derived

$$0 = m\ddot{x}_1 - K_{s_V}(r_0 - x_1) + K_{s_H}x_1 + \frac{1}{2}\dot{y}_1\left(\frac{B_{d_V}((r_0 - x_1)^2 - y_1^2)}{(r_0 - x_1)^2 + y_1^2}\right)$$
$$- \dot{x}_1\left(\frac{B_{d_H}x_1^2}{(r_1 - y_1)^2 + x_1^2} - \frac{B_{d_V}y_1(r_0 - x_1)}{(r_0 - x_1)^2 + y_1^2}\right) - \xi_x \tag{4.48}$$

$$0 = m\ddot{y}_1 + K_{s_V}y_1 - K_{s_H}(r_1 - y_1) + \frac{1}{2}\dot{x}_1\left(\frac{B_{d_V}((r_0 - x_1)^2 - y_1^2)}{(r_0 - x_1)^2 + y_1^2}\right)$$
$$+ \dot{y}_1\left(\frac{B_{d_H}(r_1 - y_1)^2}{(r_1 - y_1)^2 + x_1^2} - \frac{B_{d_V}y_1(r_0 - x_1)}{(r_0 - x_1)^2 + y_1^2}\right) - \xi_y \tag{4.49}$$

$$0 = I\ddot{\theta}_1 - \xi_\theta \tag{4.50}$$

4.4   Model for three link swimmer

The model presented in this section describes a three-link swimmer (TLS), with rotation springs and dampers between the links. First a overview of the model is presented, then the Lagrangian equations of motion are derived.

4.4.1   Model overview

The system is presented in fig. 4.4. As seen in section section 4.2, the spring connecting the first link to the cylinder yields complicated dynamics. To mitigate this when adding a third link, the first link is assumed to remain fixed in place. The first

link does interact with the fluid, but because it cant be moved, the forces that are exerted on the link will not be considered when deriving the equations of motion. Furthermore this allows for analysis of the two energy harvesting dampers in the swimmer. The links are connected through rotational springs and dampers, as before.
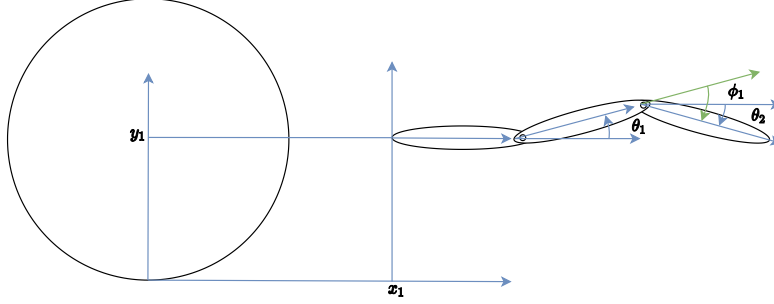

Figure 4.4: Overview of three link swimmer

The distance from the inertial frame to the tip of the first link is given by x_1 and y_1. Furthermore the rotation of the second and third link is given by θ_1 and θ_2. This gives the following global coordinates for each link

$$\vartheta_1 = \begin{bmatrix} x_1, & y_1, & 0 \end{bmatrix}, \tag{4.51}$$

$$\vartheta_2 = \begin{bmatrix} x_2, & y_2, & \theta_1 \end{bmatrix}, \tag{4.52}$$

$$\vartheta_3 = \begin{bmatrix} x_3, & y_3, & \theta_2 \end{bmatrix}. \tag{4.53}$$

The relative joint angle is defined as

$$\phi_1 = \theta_2 - \theta_1 \tag{4.54}$$

The energy dissipated in the two rotational dampers is considered when assessing the energy harvesting capabilities of the system.

4.4.2 Equations of motion

The forward kinematics for the global coordinates for the second and third links are given by

$$P_2 = \begin{bmatrix} x_1 + l_1, & y_1, & \theta_1 \end{bmatrix}^T, \tag{4.55}$$

$$\boldsymbol{P}_3 = \begin{bmatrix} x_1 + l_1 + l_2 \cos \theta_1 \\ y_1 + l_2 \sin \theta_1 \\ \theta_1 + \phi_1 \end{bmatrix}. \tag{4.56}$$

Where l_1, l_2 and l_3 are the lengths of each link respectively. Furthermore the velocity of the second and third link is found by calculating the time derivative of the position in the inertial frame

$$\boldsymbol{V}_2 = \begin{bmatrix} 0, & 0, & \dot{\theta}_1 \end{bmatrix}^T, \tag{4.57}$$

$$\boldsymbol{V}_3 = \begin{bmatrix} -l_2 \dot{\theta}_1 \sin \theta_1 \\ l_2 \dot{\theta}_1 \cos \theta_1 \\ \dot{\theta}_1 + \dot{\phi}_1 \end{bmatrix}. \tag{4.58}$$

The forward kinematics are not derived for the immovable first link. The generalized coordinates are selected as shown in fig. 4.4, which gives

$$\varphi = \begin{bmatrix} \theta_1, & \phi_1 \end{bmatrix}^T. \tag{4.59}$$

The equations of motion are derived by following the approach in section 4.2.2. First the potential energy of the system is given by the rotational springs between the joints

$$V(\varphi) = \frac{1}{2} K_{r_1} \theta_1^2 + \frac{1}{2} K_{r_2} \phi_1^2. \tag{4.60}$$

While the damping forces are given by eq. (4.12), where the $B(\varphi)$ matrix is given by

$$\boldsymbol{B}(\varphi) = \begin{bmatrix} B_{r_1} & 0 \\ 0 & B_{r_2} \end{bmatrix} \tag{4.61}$$

Furthermore the Jacobians for the second and third link are given by

$$\boldsymbol{J}_1(\varphi) = \begin{bmatrix} 0 & 0 \\ 0 & 0 \\ 1 & 0 \end{bmatrix}, \tag{4.62}$$

$$\boldsymbol{J}_2(\varphi) = \begin{bmatrix} l_2 \sin \varphi_1 & 0 \\ l_2 \cos \varphi_1 & 0 \\ 1 & 1 \end{bmatrix}. \tag{4.63}$$

While the rigid body mass matrices are given by

$$\boldsymbol{M}_1 = \begin{bmatrix} m_2 & 0 & 0 \\ 0 & m_2 & m_2\frac{1}{2}l_2 \\ 0 & m_2\frac{1}{2}l_2 & I \end{bmatrix}, \tag{4.64}$$

$$\boldsymbol{M}_2 = \begin{bmatrix} m_3 & 0 & 0 \\ 0 & m_3 & m_3\frac{1}{3}l_3 \\ 0 & m_3\frac{1}{2}l_3 & I \end{bmatrix}. \tag{4.65}$$

The equations of motion are then derived by using the Euler-Lagrange formulation as presented in eq. (4.13). After performing the calculations and simplifications the following equations of motion are derived

$$\begin{aligned} 0 = {}& I\ddot{\phi}_1 + 2I\ddot{\theta}_1 + l_2^2 m_3 \ddot{\theta}_1 + \frac{1}{2}l_2 l_3 m_3 \ddot{\phi}_1 \cos\phi_1 - \frac{1}{2}l_2 l_3 m_3 \dot{\phi}_1^2 \sin\phi_1 \\ & + l_2 l_3 m_3 \ddot{\theta}_1 \cos\phi_1 - l_2 l_3 m_3 \dot{\theta}_1 \dot{\phi}_1 \sin\phi_1 + K_{r_1}\theta_1 + B_{r_1}\dot{\theta}_1 - \xi_{\theta_1} \end{aligned} \tag{4.66}$$

$$\begin{aligned} 0 = {}& I\ddot{\phi}_1 + I\ddot{\theta}_1 + \frac{1}{2}l_2 l_3 m_3 \ddot{\theta}_1 \cos\phi_1 - \frac{1}{2}l_2 l_3 m_3 \dot{\theta}_1 \dot{\phi}_1 \sin\phi_1 + K_{r_1}\phi_1 \\ & + \frac{1}{2}l_2 l_3 m_3 \dot{\theta}_1 \sin\theta_1 + \frac{1}{2}l_2 l_3 m_3 \dot{\phi}_1 \dot{\theta}_1 \sin\phi_1 + B_{r_2}\dot{\phi}_1 - \xi_{\phi_1} \end{aligned} \tag{4.67}$$

4.5 Modified three link swimmer

The three link swimmer is also implemented with the simulator presented in Gazzola et al. (2011) and Bernier et al. (2019), and will be referred to as the modified three link swimmer (MTLS). The main differences in this model is that the links are separated from each other and connected with linear springs. A model overview will be presented and then the equations of motion will be derived.

4.5.1 Overview of model

The model is shown in fig. 4.5: the links are separated such that the fluid can flow between them. Furthermore, the linear and rotational dampers are removed from the model while linear springs are added between the links. The first link is movable, but it is constrained with a spring connected to the centre of the cylinder. The springs between the links are connected to the front of each link, as shown in the illustration.
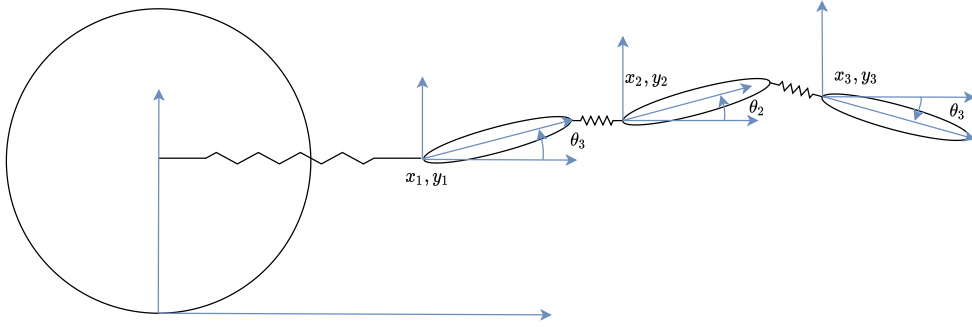
Figure 4.5: Overview of MTLS

The position of the front of each link is given by $[x_i, y_i]^T$ and the rotations are given by θ_i. The global coordinates are then given by

$$\boldsymbol{\vartheta}_1 = \left[x_1, \ y_1, \ \theta_1 \right], \tag{4.68}$$

$$\boldsymbol{\vartheta}_2 = \left[x_2, \ y_2, \ \theta_2 \right], \tag{4.69}$$

$$\boldsymbol{\vartheta}_3 = \left[x_3, \ y_3, \ \theta_3 \right]. \tag{4.70}$$

The energy harvesting capability of the model is not measured. This model is compared to the models developed in COMSOL to investigate and highlight problems which might arise with the simulations.

4.5.2   Equations of motion

The links are not relatively constrained, hence the forward kinematics can be expressed as the global coordinates

$$\boldsymbol{P}_1 = \left[x_1, \ y_1, \ \theta_1 \right]^T, \tag{4.71}$$

$$\boldsymbol{P}_2 = \left[x_2, \ y_2, \ \theta_2 \right]^T, \tag{4.72}$$

$$\boldsymbol{P}_1 = \left[x_3, \ y_3, \ \theta_3 \right]^T, \tag{4.73}$$

Furthermore, the velocity of the links can be found by calculating the time derivative of the position in the inertial frame

$$V_1 = \begin{bmatrix} \dot{x}_1, & \dot{y}_1, & \dot{\theta}_1 \end{bmatrix}^T, \tag{4.74}$$

$$V_2 = \begin{bmatrix} \dot{x}_2, & \dot{y}_2, & \dot{\theta}_2 \end{bmatrix}^T, \tag{4.75}$$

$$V_3 = \begin{bmatrix} \dot{x}_3, & \dot{y}_3, & \dot{\theta}_3 \end{bmatrix}^T, \tag{4.76}$$

The generalized coordinates are then chosen as

$$\varphi = \begin{bmatrix} x_1, & y_1, & \theta_1, & x_2, & y_2, & \theta_2, & x_3, & y_3, & \theta_3 \end{bmatrix}^T. \tag{4.77}$$

The length of the springs can then be expressed with the generalized coordinates on the form

$$\chi_1(\varphi) = \sqrt{x_1^2 + y_1^2}, \tag{4.78}$$

$$\chi_2(\varphi) = \sqrt{x_2^2 + y_2^2} - \left(\sqrt{(l_1 \cos \theta_1 + x_1)^2 + (l_1 \sin \theta_1 + y_1)^2} \right), \tag{4.79}$$

$$\chi_3(\varphi) = \sqrt{x_3^2 + y_3^2} - \left(\sqrt{(l_2 \cos \theta_2 + x_2)^2 + (l_2 \sin \theta_1 + y_2)^2} \right), \tag{4.80}$$

where l_1 and l_2 are the lengths of the links. By using eq. (4.8) and eq. (4.6) the Jacobians and body frame velocities can be derived. Due to the size of these matrices they are given in appendix A. Furthermore, the mass matrices are given by

$$M_i = \begin{bmatrix} m_i & 0 & 0 \\ 0 & m_i & m_i \frac{1}{2} l_i \\ 0 & m_i \frac{1}{2} l_i & I \end{bmatrix}. \tag{4.81}$$

While the potential energy of the system is given by

$$V(\varphi) = \frac{1}{2} K_{s_1} (r_0 - \chi_1(\varphi))^2 + \frac{1}{2} K_{s_2} (r_1 - \chi_2(\varphi))^2 + \frac{1}{2} K_{s_3} (r_2 - \chi_3(\varphi))^2 \tag{4.82}$$

where r_i are the resting configurations of the linear springs. The kinetic energy is given by eq. (4.5). Combining these yields the Lagrangian shown in eq. (4.10). The equations of motion can now be derived by using the Euler-Lagrange equation given in eq. (4.13). It is seen from the Jacobians in appendix A that the bodies are not relatively constrained, therefore the equations of motion are three sets of equations

with the springs acting as forces, that can be solved independently for each rigid body. These equations are solved online during the simulations, and will not be stated in this thesis.

Chapter 5

Building the simulation models

In this chapter the methods used to build the models presented in chapter 4 are discussed. The first three models are built in COMSOL Multiphysics and the required modules are the CFD module with the single-phase flow interface (spf), Multibody Dynamics module with the multibody modelling inteferface (mbd). The fourth model is implemented in the simulator presented in Gazzola et al. (2011), where the parameters were adjusted and the number of links were customized for the purposes of this thesis.

5.1 COMSOL models

The models built in COMSOL share a common environment with a cylinder in a constant fluid flow. In this section the methods for implementing the environment and submerged objects in COMSOL are presented.

5.1.1 Building fluid domain and cylinder

The whole fluid domain, the two-dimensional view of the cylinder, and the small region behind the cylinder are represented using a large rectangle, a circle and a smaller rectangle respectively, as shown in figure fig. 5.1. The circle is modeled as a hole in the two-dimensional domain given by the largest rectangle. The submerged objects are placed close to the circle inside the smaller rectangle. The mesh used for the FEM is divided two separate sub-meshes. The first is a coarser rectangular mesh for the large rectangle where the mesh becomes coarser the further away from the cylinder it is, while the second is a finer triangular mesh covering the small rectangle containing the models.

The wake behind the cylinder is expected to induce large movements in the submerged objects, hence the mesh in the smaller rectangle is selected to be deforming, which allows it to adapt as the models move. The rest of the mesh is rigid.

The inlet lies to the the left side of the fluid domain, where the inflow has a mean velocity of 2 m/s and has a fully developed velocity profile. The right side is selected as the outlet. A slip condition is imposed on the upper and lower edges of the domain, acting as friction-less walls. The boundary between the circle and the fluid domain is selected to have a no-slip condition, which is necessary for the vortex street to form.
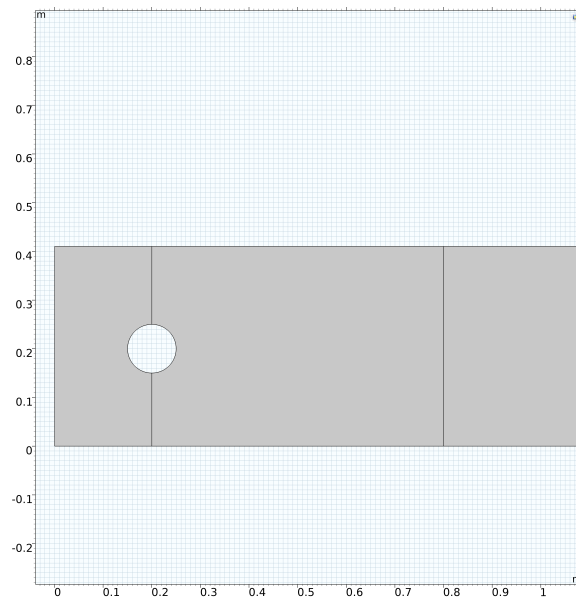
Figure 5.1: Overview of fluid domain with cylinder

5.1.2   Double pendulum with spring and damper

The DP is implemented as shown in fig. 5.2. The geometrical shapes are given by two overlapping rectangles which represent the links of the DP. By using the Multibody dynamics module, a rotational hinge with a spring and damper is added in the overlapping region to connect the two links. Furthermore a linear spring and damper are added between the circle and the first link, but these are not visible because they don't interact with the fluid. The material of the links is selected to be stainless steel, which is denser than water, but the forces from the passing vortices are expected to be much higher than the buoyancy forces. The parameters for the simulation are selected as shown in table 5.1. The spring constant K_{s_1} is selected

to be very large, compared to the other parameters. This is done to constrain the position of the DP in the horizontal direction.

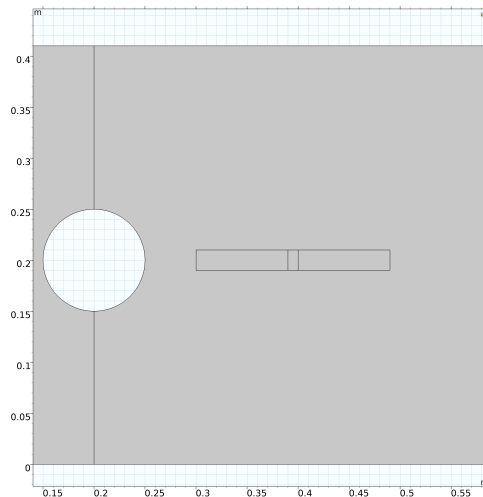| Parameter	Value	Unit
K_{l_1}	50000	N/m
B_{l_1}	2	Ns/m
K_{r_1}	10	Nm/rad
B_{r_1}	1	Nms/rad

Table 5.1: Parameters for DP in COMSOL

Figure 5.2: Overview of double pendulum COMSOL simulation

5.1.3   Block with two springs and two dampers

The COMSOL model of the BSD is shown in fig. 5.3. The geometrical shape of the BSD is given as a square, where the edges are smoothed. Using the Multibody dynamics module, a horizontal spring and damper are attached from the centre of the block to the centre of the circle, and a vertical spring and damper are coupled between the centre of the BSD and the lower wall. The material for the block is selected to be the same as the DP in section 5.1.2. The parameters for the springs and dampers are selected as shown in table 5.2.

Parameter	Value	Unit
K_{s_H}	1000	N/m
B_{d_H}	50	Ns/m
K_{s_V}	10	N/m
B_{d_V}	2	Ns/m

Table 5.2: Parameters for block with two springs and two dampers in COMSOL
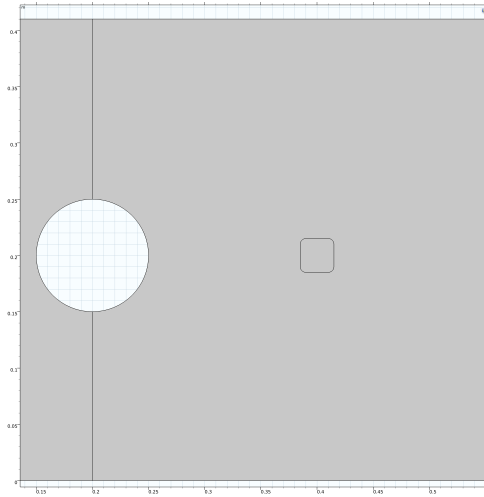
Figure 5.3: Overview of block with two springs and two dampers COMSOL simulation

5.1.4   Three link swimmer

The three link swimmer in COMSOL is shown in fig. 5.4. The links are modelled as overlapping ellipses. The Multibody-dynamics module allows the first link to be constrained, which enables FSI but the link is immovable. Furthermore rotational springs and dampers are added at the overlapping area between each link. The material for the links is selected to be the same as in section 5.1.2. Finally the parameters for the TLS are given in table 5.3.

Parameter	Value	Unit
K_{r_1}	15	Nm/rad
B_{r_1}	5	Nms/rad
K_{r_2}	15	Nm/rad
B_{r_2}	5	**Nms/rad**

Table 5.3: Parameters for three linked swimmer in COMSOL
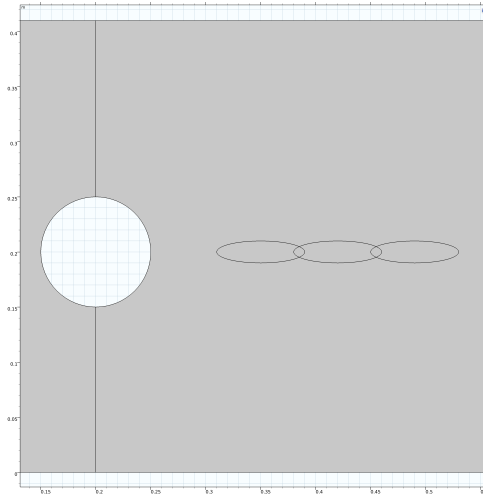
Figure 5.4: Overview of a three linked swimmer in COMSOL

5.2 Dimensionless simulation of the modified three link swimmer

In this section the simulation of the dimensionless simulation of the MTLS is presented and the relevant equations are shown.

The dimensionless Reynolds number is often used to characterize a fluid flow in a simulation. By the use of dimensional analysis, the number of variables that describe the system can be reduced. Some parameters can then be adjusted while the Reynolds number remains constant by altering other variables such as fluid velocity and cylinder diameter, thereby preserving the properties of the fluid, which allows for analysis of how the model behaves at certain Reynolds numbers without having to consider the size of the model. The simulator developed in Gazzola et al. (2011), was set to preserve $Re = 200$ for the model studied in this thesis. By using eq. (3.8)

the following relation is found

$$200 = \frac{DU_\infty}{\nu}.,$$ (5.1)

where the kinematic viscosity is selected to be $0.0004 \text{ m}^2/s$. This is much higher than for water, which is approximately $0.89 \cdot 10^{-6} \text{ m}^2/s$. By using the value for water, the vortex shedding occurs very slowly, and the vortices are shed with a very small frequency. To maintain $Re = 200$ this would imply a very long simulation to get valuable information and access to much more computational power would be needed. Therefore the kinematic viscosity is increased, allowing for faster shedding frequencies, which results in data being generated faster.

The simulations is a one by one dimensionless environment, where the sizes of the cylinder and submerged bodies are altered by adjusting a parameter r, which is the characteristic length to environment ratio. The characteristic length of a cylinder is the diameter, while for an ellipse it is the longest distance between two points. To simulate the model presented in this thesis $r = 0.04$ is selected for both the cylinder and swimmer links. While the links are separated by 0.045 and the resting configuration of the linear springs is selected to be 0.02. The solid bodies are by default neutrally buoyant.

After running the simulation it is necessary to scale the system to a desired size. The cylinders developed in COMSOL have a diameter of 0.1 m. The following dimensionless variables are introduced, based on the theory presented in Gazzola et al. (2011) and Bernier et al. (2019)

$$t^* = \frac{tU_\infty}{D},$$ (5.2)

$$x^* = x/r_d,$$ (5.3)

$$y^* = y/r_d,$$ (5.4)

$$\text{(5.5)}$$

$$k_{l_i}^* = \frac{2k_{l_i}}{\rho U_\infty^2},$$ (5.6)

where t^* is the non-dimensional time, $[x^*, \ y^*]^T$ are the dimensionless position coordinates, $k_{l_i}^*$ is the non-dimensional spring stiffness coefficient of link i, and r_d is the ratio of cylinder size to desired cylinder size. Furthermore, by using eq. (5.1), the fluid velocity is found to be 0.8 m/s. The spring stiffness is selected to be $k_{l_i}^* = 30$,

and when scaled to our desired values, it is $k_{l_i} = 9571$ N/m.

For a more detailed overview of the simulator used in this thesis the reader is referred to Gazzola et al. (2011).

Chapter 6

Position control for underwater snake robots

In this chapter the theory and method for developing a controller for a snake robot to hold a determined position is presented. First, a simplified model of a snake robot is shown, then the integral line of sight guidance law presented in Kohl et al. (2016) is combined with a PID controller for forward velocity to achieve a position hold controller.

6.1 Control-oriented model

A detailed model that considers the full kinematics and dynamics of a planar snake robot with revolute joints is presented in Kelasidi, Pettersen, Gravdahl and Liljeback (2014). However, the complexity of this model makes it inappropriate for the design of control systems and motion planning. A simplified model of the planar snake robot locomotion is developed in Liljebäck et al. (2013), and is further extended to underwater snake robots without ocean currents in Kelasidi, Pettersen and Gravdahl (2014). Currents where included in the control-oriented model presented in Kohl et al. (2015b), with the following assumptions

Assumption 6.1 ((Kohl et al.; 2015b, Assumption 1)) *The drag coefficient in the normal direction is larger than in the tangential direction, $c_n > c_t$.*

Assumption 6.2 ((Kohl et al.; 2015b, Assumption 2)) *The underwater snake robot is moving slowly by using lateral undulations for forward propulsion and limited link angles.*

The model is further simplified and validated through extensive simulation studies in Kohl et al. (2015a). The control-oriented model derived in these papers is given by

$$\dot{\boldsymbol{\phi}} = \mathbf{v}_\phi \tag{6.1}$$

$$\dot{\theta} = v_\theta \tag{6.2}$$

$$\dot{p}_x = v_t \sin\theta - v_n \sin\theta \tag{6.3}$$

$$\dot{p}_y = v_t \sin\theta + v_n \cos\theta \tag{6.4}$$

$$\mathbf{v}_\phi = \bar{\boldsymbol{u}} \tag{6.5}$$

$$\dot{v}_\theta = -\lambda_1 v_\theta + \frac{\lambda_2}{N-1} v_{t,\text{rel}} \bar{\boldsymbol{e}}^T \boldsymbol{\phi} \tag{6.6}$$

$$\dot{v}_t = -\frac{c_t}{m} v_{t,\text{rel}} + \frac{2c_p}{Nm} \bar{\boldsymbol{e}}^T \boldsymbol{\phi} v_{n,\text{rel}} - \frac{c_p}{Nm} \boldsymbol{\phi}^T \boldsymbol{A} \bar{\boldsymbol{D}} \mathbf{v}_\phi \tag{6.7}$$

$$\dot{v}_n = \frac{2c_p}{Nm} \bar{\boldsymbol{e}}^T \boldsymbol{\phi} v_{t,\text{rel}} - \frac{c_n}{m} v_{n,\text{rel}}. \tag{6.8}$$

Where $\boldsymbol{\phi}$ contains all the relative $N-1$ joint angles ϕ_i for all joints except the first, while λ_i are constants that characterize the rotational dynamics. Furthermore the heading of the snake robot is denoted by θ. The tangential and normal velocities are given by v_t and v_n respectively, while the relative velocities are given as $v_{t,\text{rel}}$ and $v_{n,\text{rel}}$. The c_t, c_n coefficients represent the drag in the tangential and normal directions respectively, while c_p is the propulsion coefficient. The summation vector is denoted as $\bar{e} = [1, \dots 1]^T \in \mathbb{R}^{N-1}$, and the matrix $\bar{D} = D^T(DD^T)^{-1}$. The A and D are given by

$$D = \begin{bmatrix} 1 & -1 & & \\ & \ddots & \ddots & \\ & & 1 & -1 \end{bmatrix}, \tag{6.9}$$

$$A = \begin{bmatrix} 1 & 1 & & \\ & \ddots & \ddots & \\ & & 1 & 1 \end{bmatrix}. \tag{6.10}$$

6.2 Control system

To achieve a forward motion, the gait controller presented in Kohl et al. (2015a) is used:

$$\bar{\boldsymbol{u}} = \ddot{\boldsymbol{\phi}}_{\text{ref}} + k_{v_\phi}(\dot{\boldsymbol{\phi}}_{\text{ref}} - \dot{\boldsymbol{\phi}}) + k_\phi(\boldsymbol{\phi}_{\text{ref}} - \boldsymbol{\phi}). \tag{6.11}$$

Where $k_{v_\phi}, k_\phi > 0$ are the control gains. Inserting eq. (6.11) into eq. (6.5) gives the following dynamics

$$\ddot{\tilde{\phi}} + k_{v_\phi}\dot{\tilde{\phi}} + k_\phi\tilde{\phi} = 0. \tag{6.12}$$

Which is uniformly globally exponentially stable as stated in Kohl et al. (2016). Forward propulsion is attained by using the sinusoidal gate given by

$$\phi_{i,\,\text{ref}} = \alpha g(i)\sin(\omega t + (i-1)\delta) + \phi_0, \tag{6.13}$$

where α is the amplitude, $g(i)$ is a scaling constant that scales the amplitude of each joint, ω is the frequency of the sinusoidal motion and ϕ_0 is a constant offset that induces turning. By modifying the turning offset a desired heading can be attained as shown in Liljeback et al. (2012). The new turning offset is given by

$$\phi_0 = \frac{1}{\lambda_2 v_{t,\text{rel}}}\left[\ddot{\theta}_{\text{ref}} + \lambda_1\dot{\theta}_{\text{ref}} - k_\theta\tilde{\theta}\right] - \frac{\lambda_2}{N-1}v_{t,\text{rel}}\sum_{i=1}^{N-1}\alpha g(i)\sin(\omega t + (i-1)\delta). \tag{6.14}$$

by inserting $\phi = \tilde{\phi} + \phi_{\text{ref}}$ into eq. (6.6) gives the following error dynamics for the heading angle

$$\ddot{\tilde{\theta}} + \lambda_1\dot{\tilde{\theta}} + k_\theta\tilde{\theta} = \frac{\lambda_2}{N-1}v_{t,\text{rel}}\bar{e}^T\tilde{\phi}. \tag{6.15}$$

From eq. (6.12) it is apparent that that $\tilde{\phi}$ goes to zero, implying that $\tilde{\theta}$ also goes to zero.

6.3 Integral line of sight

For traditional Line-of-Sight (LOS) guidance, the desired heading angle, θ_{ref}, is given by

$$\theta_{\text{ref}} = -\tan^{-1}\left(\frac{y}{\Delta}\right), \quad \Delta > 0. \tag{6.16}$$

Where y is the distance from the snake robot to the desired path along $y = 0$ and Δ is the distance to a point on the path that coincides with the heading of the robot, called the look-ahead distance. If the snake robot is able to track the heading angle given by the LOS guidance law, it can be shown that the snake robot converges to and follows the desired path, under the assumption that there are no external disturbances. For the purposes of this thesis, the snake robot has to operate in conditions where external disturbances are present in the form of ocean currents. This issue was first addressed with Integral Line-Of-Sight (ILOS) guidance for marine surface vessels in Borhaug et al. (2008) and later implemented for underwater snake robots in Kohl

et al. (2016). This is achieved by extending the traditional LOS guidance law, by adding integral action. The new desired heading angle is given by

$$\theta_{\text{ref}} = -\tan^{-1}\left(\frac{y + \delta y_{\text{int}}}{\Delta}\right), \quad \Delta > 0, \tag{6.17}$$

$$\dot{y}_{\text{int}} = \frac{\Delta y}{(y + \delta y_{\text{int}})^2 + \Delta^2}. \tag{6.18}$$

From eq. (6.16) it is apparent that the desired heading goes to zero as the snake robot reaches the desired trajectory. This is not desirable when there are external disturbances present. The ILOS guidance law in eq. (6.19) allows the desired heading to be nonzero at the desired path and sustain it in the presence of constant disturbances. The ILOS gudance law for the underwater snake robot is illustrated in fig. 6.1. The
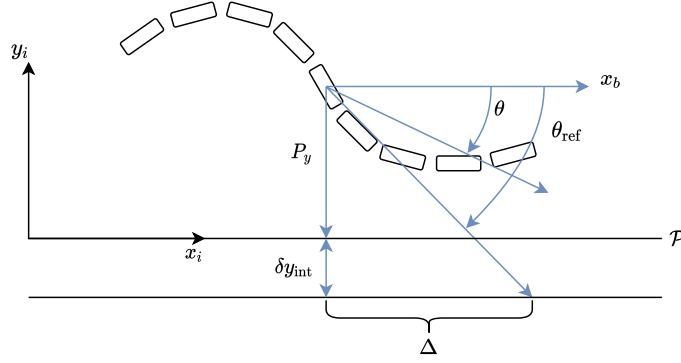
Figure 6.1: Integral Line-Of-Sight

convergence to the desired path for underwater snake robots is proven in Kohl et al. (2016), under the following assumptions

Assumption 6.3 ((Kohl et al.; 2016, Assumption 1)) *The ocean current* $[V_x, V_y]$ *is constant and irrotational in the inertial frame, furthermore it is bounded by* $V_{c,\ max} \geq \sqrt{V_x^2 + V_y^2}$.

Assumption 6.4 ((Kohl et al.; 2016, Assumption 2)) *The relative forward velocity* $v_{r,\ rel}$ *is upper and lower bounded by* V_{max} *and* V_{min} *such that* $V_{max} \geq V_{min} > 0$.

Assumption 6.5 ((Kohl et al.; 2016, Assumption 3)) *The forward velocity is large enough to compensate for the current,* $V_{min} > V_{c,\ max}$.

6.4 Position hold control

To hold a constant position, the ILOS guidance law presented in section 6.3 has to be modified to track a desired y position. The following modification is suggested

$$\theta_{\text{ref}} = -\tan^{-1}\left(\frac{\tilde{y} + \delta\tilde{y}_{\text{int}}}{\Delta}\right), \quad \Delta > 0, \tag{6.19}$$

$$\dot{\tilde{y}}_{\text{int}} = \frac{\Delta\tilde{y}}{(\tilde{y} + \delta\tilde{y}_{\text{int}})^2 + \Delta^2}. \tag{6.20}$$

Where $\tilde{y} = y - y_{\text{ref}}$. Setting $y_{\text{ref}} = 0$ gives the original ILOS guidance law in eq. (6.19). The proof of convergence presented in Kohl et al. (2016) is still valid with this minor modification, because it only affects the distance to the desired path.

To attain a desired position in the horizontal direction, a controller for the gait given by eq. (6.13) can be used. This problem is addressed in Bernier et al. (2019) by using a PI controller with an anti-windup loop for the amplitude α. It is shown by Kohl et al. (2015a), that the averaged velocity $\mathbf{v}_{\text{av}}$ converges to

$$\mathbf{v}_{\text{av}} = \alpha^2\omega k_\delta \begin{bmatrix} \dfrac{Nc_nc_p}{2(c_nc_tN^2 - 4(N-1)^2c_p^2\phi_0^2)} \\ \dfrac{c_p^2\phi_0(N-1)}{c_nc_tN^2 - 4(N-1)^2c_p^2\phi_0^2} \\ \dfrac{Nc_nc_p\lambda_2\phi_0}{2\lambda_1(c_nc_tN^2 - 4(N-1)^2c_p^2\phi_0^2)} \end{bmatrix} + \begin{bmatrix} V_t \\ V_n \\ 0 \end{bmatrix}. \tag{6.21}$$

Where k_δ is the proportional dependence on δ, and V_t, V_n are the tangential and normal body frame components of the current. The average velocity is quadratic with the amplitude. By using the frequency ω rather than the amplitude for position control, a linear relationship between the average velocity and PID controller can be achieved. Therefore the horizontal position of the underwater snake robot may be controlled by adjusting the frequency of the gait given in eq. (6.13). The position controller implemented in this thesis is given by

$$\omega = K_{p_\omega}\tilde{x} + K_{d_\omega}\dot{\tilde{x}} + K_{i_\omega}\int_0^t \tilde{x}d\tau. \tag{6.22}$$

Where $\tilde{x} = x_{\text{ref}} - x$ and the tuning parameters are given by $K_{p_\omega} > 0, K_{d_\omega} > 0, K_{i_\omega} > 0$.

6.5   Integrator windup

The limits of the physical actuators are modeled as a saturation. This might lead to integral windup, which severely affects the performance of the PID controller in the case of disturbances and nonlinear dynamics. To avoid this, eq. (6.22) is extended to

$$\omega = K_{p_\omega}\tilde{x} + K_{d_\omega}\dot{\tilde{x}} + K_{i_\omega}\int_0^t \tilde{x}d\tau - \frac{1}{T_t}\int_0^t (\omega - \omega_{\text{unsat}})\,d\tau. \qquad (6.23)$$

Where ω_{unsat} is the unsaturated value of ω, and T_t is the time constant of the anti-windup chosen according to the method presented in Markaroglu et al. (2006), given by

$$T_t = \sqrt{T_i \cdot T_d}, \qquad (6.24)$$

where T_i is the integral time constant and T_d is the derivative time constant of eq. (6.23).

Chapter 7

Simulation study

The results from the simulation of the four models derived in chapter 4 are presented in this chapter. First the DP, BSD and TLS were implemented in COMSOL Multi-physics, and these results are presented first. Then the results of the MTLS which was simulated with the simulator presented in Gazzola et al. (2011) are presented. The results are then discussed, where the COMSOL models are compared and the energy harvesting is investigated, finally the COMSOL models are compared to the MTLS. Then the results for the two simulation methods are compared.

7.1   Double Pendulum

The horizontal and vertical displacement for the first and second link in the inertial frame, are shown in fig. 7.1. Furthermore, the relative angle ϕ_1 and the angular velocity are given in fig. 7.1e and fig. 7.1f. Finally, the energy dissipated in the rotational damper is given by fig. 7.2.

The first link has a slightly larger horizontal displacement then the second link, however the vertical displacement is substantially larger for the second link. The relative angle is in the range $[-30°, \ 30°]$, but the angular velocity is very high with a maximal value of approximately 1200 deg/s, which suggests a fast whipping motion. The dissipated energy is constant for approximately the first 2 seconds, then it increases steadily for the rest of the simulation time.
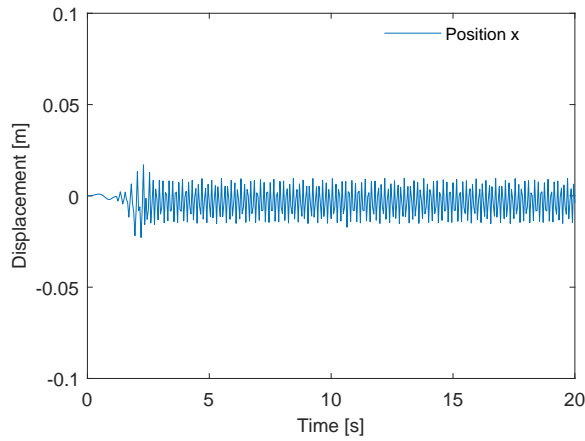
(a) Horizontal position first link.
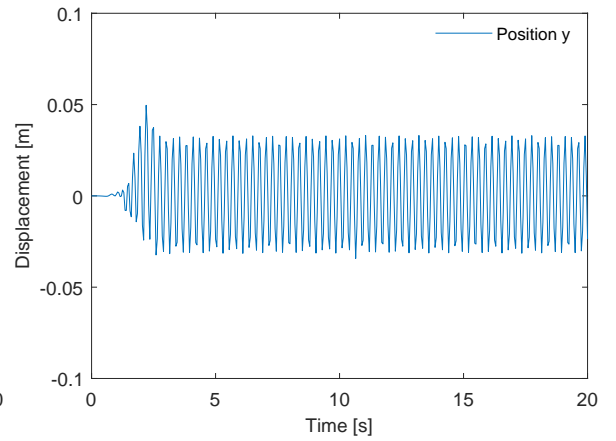
(b) Vertical position first link.
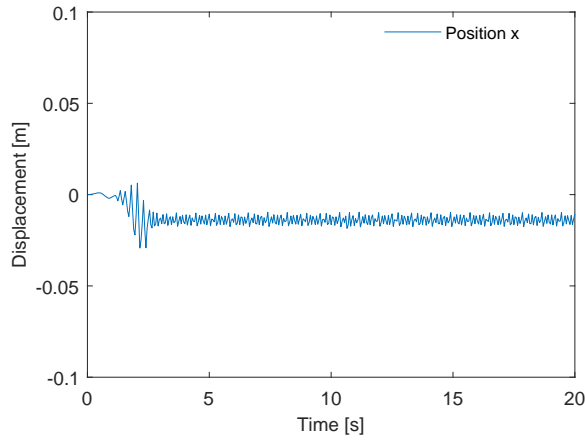
(c) Horizontal position second link.
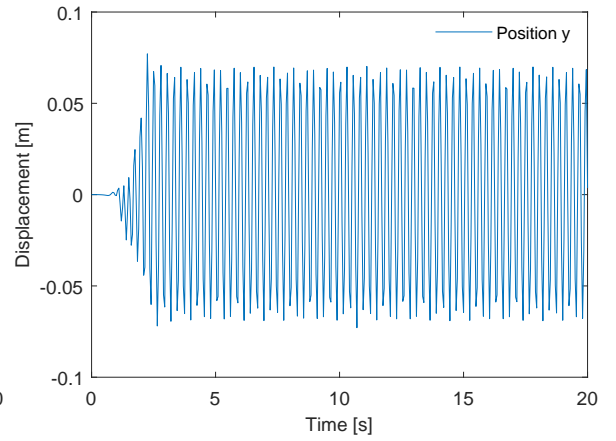
(d) Vertical position second link.
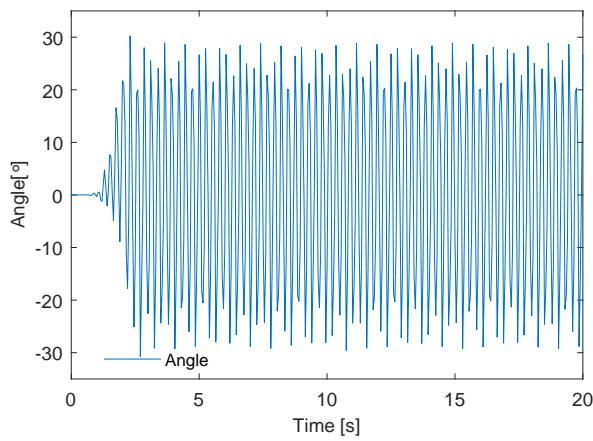
(e) Relative rotation between links.
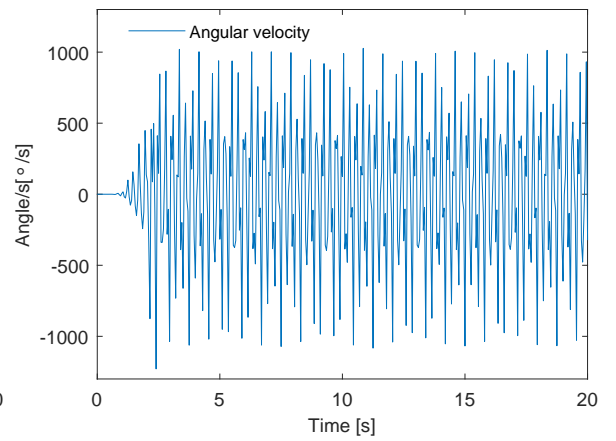
(f) Relative angular velocity between links
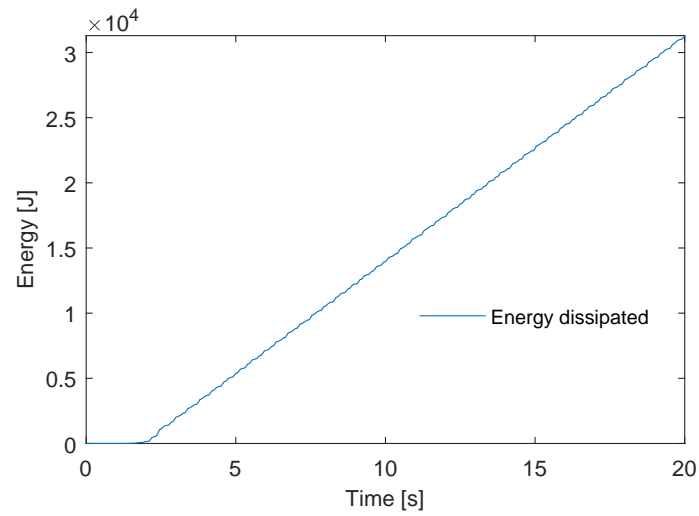
Figure 7.1: Positions and rotations of the DP

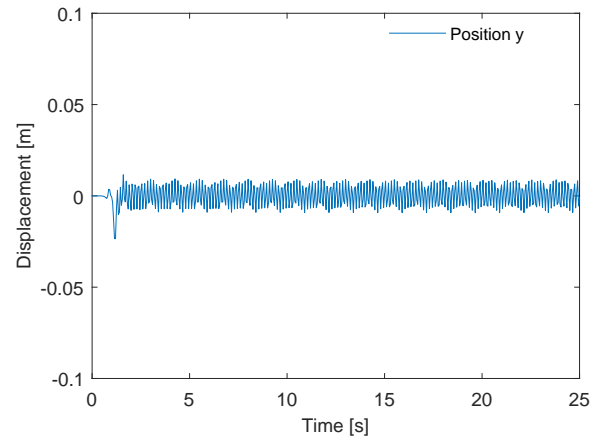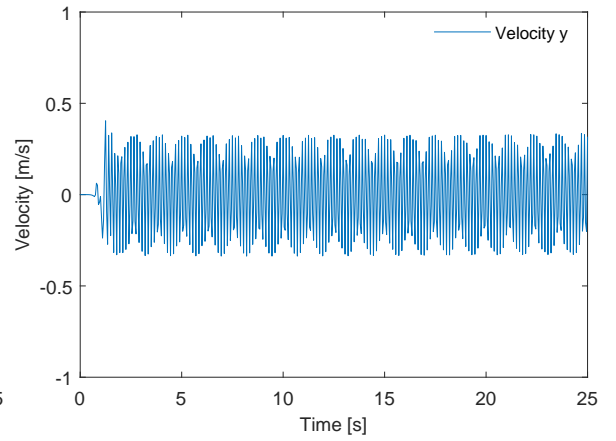**Figure 7.2:** Energy dissipated in rotational damper

7.2 Square block

The horizontal and vertical displacements and velocities of the block given in the inertial frame are shown in fig. 7.3. Furthermore the energy dissipated in the vertical damper is given in fig. 7.4.

There is a large horizontal displacement during the initial formation of the wake, but then the displacement stabilizes at about −0.05 m for the rest of the simulation time. The vertical displacement oscillates about 0 with an amplitude of approximately 0.01 m. The velocity plot reflects what is observed for the displacement, and the velocity is significantly higher in vertical direction, which is expected due to the less stiff spring. The dissipated energy increases continuously after the wake has formed at about 2 s.
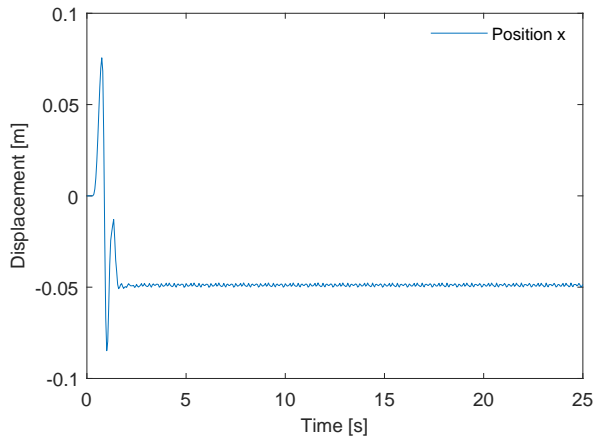
(a) Horizontal position first link.

(b) Vertical position first link.
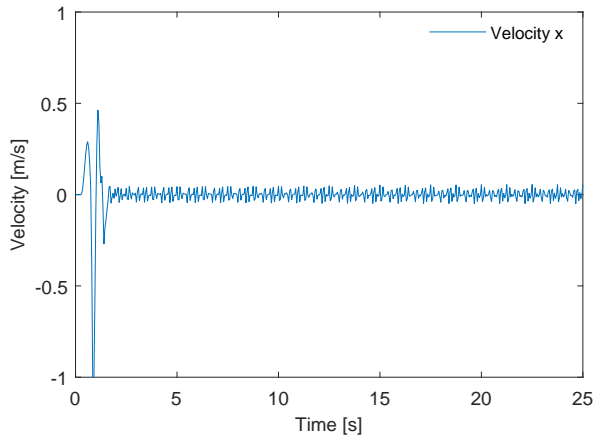
(c) Horizontal velocity second link.

(d) Vertical velocity second link.

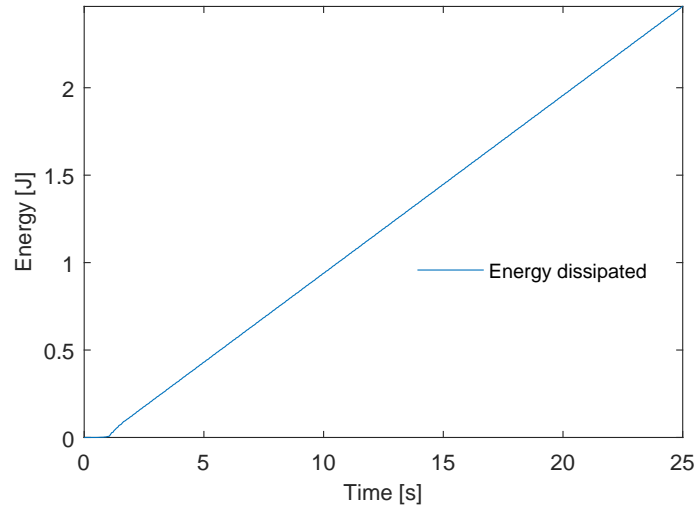**Figure 7.3:** Positions and velocities of the BSD

Figure 7.4: Energy dissipated in vertical damper

7.3   Three linked swimmer

The horizontal and vertical displacements of the first, second and third link, given in the inertial frame, are shown in fig. 7.5. The relative rotations ϕ_1 and ϕ_2 and their respective derivatives are given by fig. 7.6. Finally the energy dissipated in the dampers is shown in fig. 7.7.

It is observed that the constraints implemented on the first link are working as expected, and there is no horizontal or vertical displacement. The vertical displacements of the second and third links are both oscillating about $x = 0$ m. Due to the physical connection between the links, the motion of the second link also propagates to the third link. Therefore the third link has a significantly larger vertical displacement. The relative rotations are similar, however the second link has a significantly larger amplitude. The energy dissipated in the rotational dampers is steadily increasing after the wake has formed, but the energy dissipated by the damper between the first and second links is larger by a factor 10.
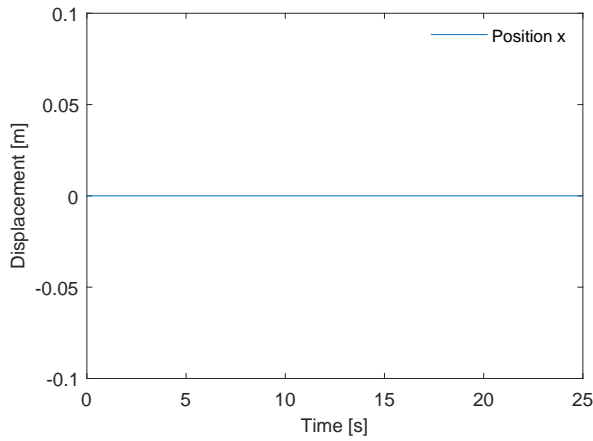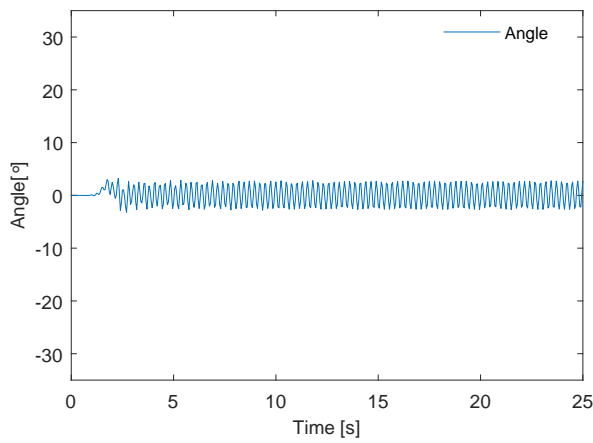
(a) Horizontal position first link.
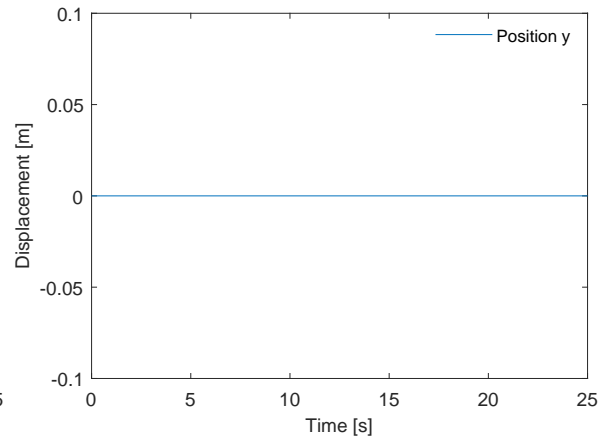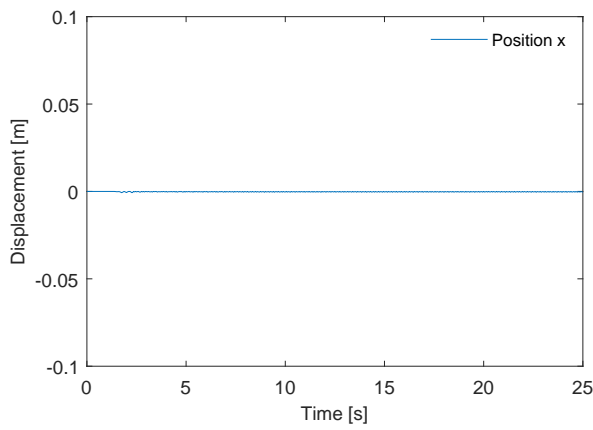
(b) Vertical position first link.

(c) Horizontal position second link.
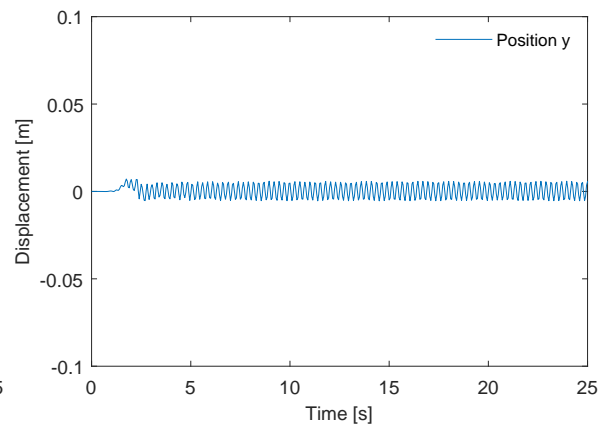
(d) Vertical position second link.
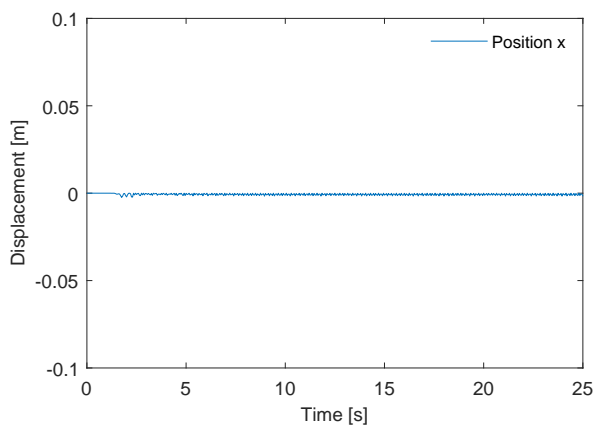
(e) Horizontal position third link.
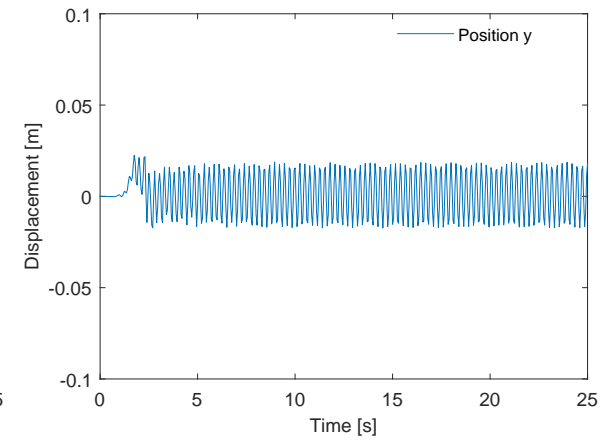
(f) Vertical position third link.

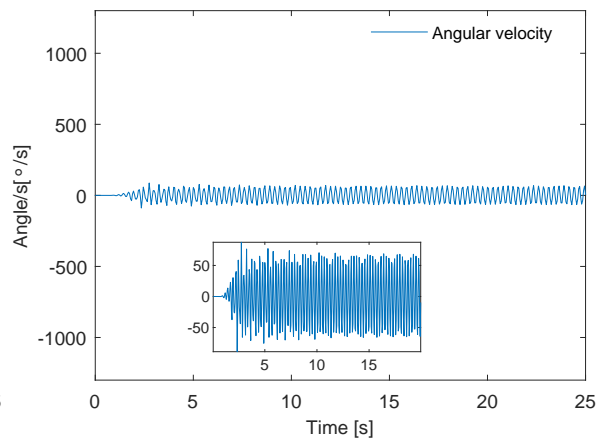**Figure 7.5:** Positions of the TLS
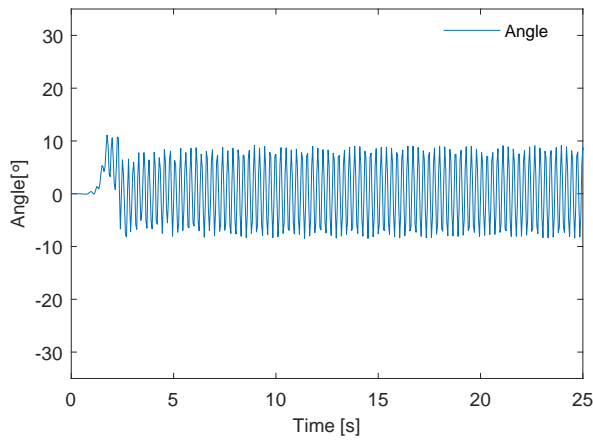
(a) Relative rotation of first and second link.
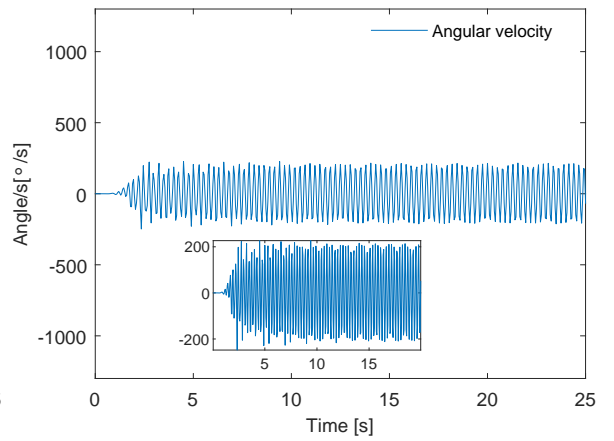
(b) Relative angular velocity between first and second link.

(c) Relative rotation of first and second link.

(d) Relative angular velocity of second and third link.

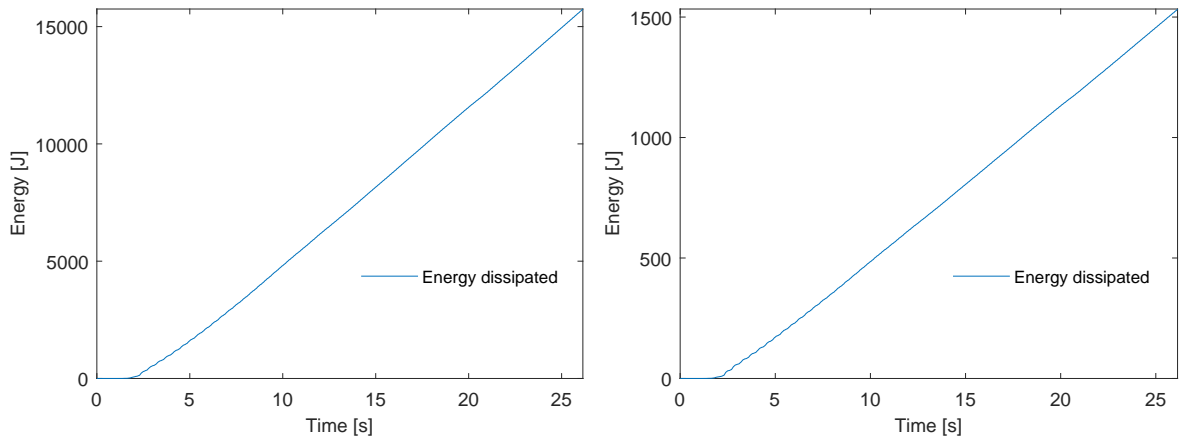**Figure 7.6:** Relative rotation and angular velocities of the TLS

Figure 7.7: Energy dissipated in the first and second damper

7.4 Simulation times

The computation time for the three models in COMSOL Multiphysics are given
in table 7.1. It is noted that the computational time of the double pendulum is
substantially longer than for both the other models.

Model	Time simulated	Computational time
Double Pendulum	20 seconds	9 hours 57 minutes 7 seconds
Block with double springs and dampers	25 seconds	2 hours 34 minutes 2 seconds
Three linked swimmer	25 seconds	2 hours 12 minutes 14 seconds

Table 7.1: Simulation time and computational time for COMSOL models

7.5 Interaction between immersed bodies and wakes

The figures in this section were generated directly from COMSOL Multiphysics.
The figures show the magnitude of the velocity of the fluid around the cylinder and
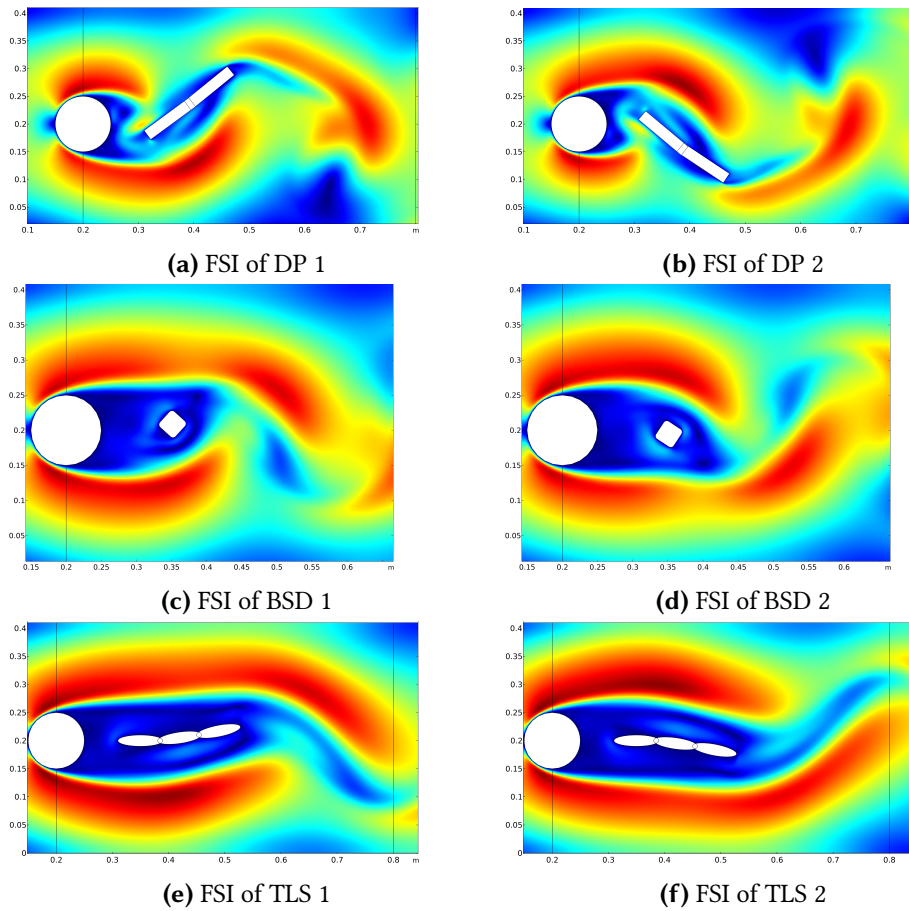submerged structures, and how the vortices are propagated past the object.

(a) FSI of DP 1

(b) FSI of DP 2

(c) FSI of BSD 1

(d) FSI of BSD 2

(e) FSI of TLS 1

(f) FSI of TLS 2

Figure 7.8: Interaction between swimmers and cylinder wake in COMSOL Multiphysics

7.6   Modified Three link swimmer results

The modified three link swimmer was simulated with the simulator presented in Gazzola et al. (2011). The results were then scaled by using the equations presented in section 5.2.

The positions of the three links are given in fig. 7.9, where it is seen that the second and third links are pulled forward before the vortex street is fully formed, then they are dragged with the fluid flow as the vortex street forms, before the springs pulls them back and they begin oscillating at about 0.03 m and 0.05 m displacements respectively. The links all oscillate about approximately 0 m, and it is observed that the amplitude is bigger the further away from the cylinder the links are. This is expected as the vortices shed increase in size as they propagate downstream. This

is also observed in the velocity and angular velocity plots in fig. 7.10, where the amplitude increases with the distance to the cylinder. It is observed that the angles of the first and second link have a large spike at 4 s in opposite directions. This is reflected in the plot of the relative angles in fig. 7.11. This happens approximately at the same time as the second and third link are dragged downstream. As the first and second links are pulled apart, a vortex is shed between them, resulting in the end of the first link being dragged upwards, while the front of the second link is pushed downwards.
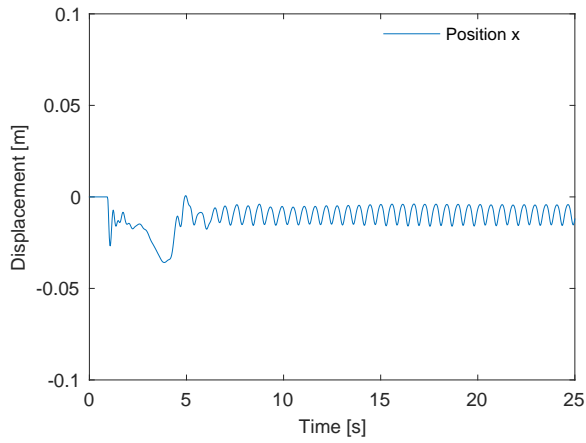
(a) Horizontal position first link.
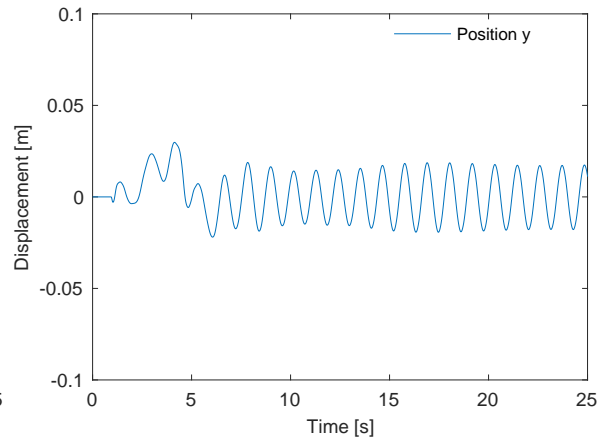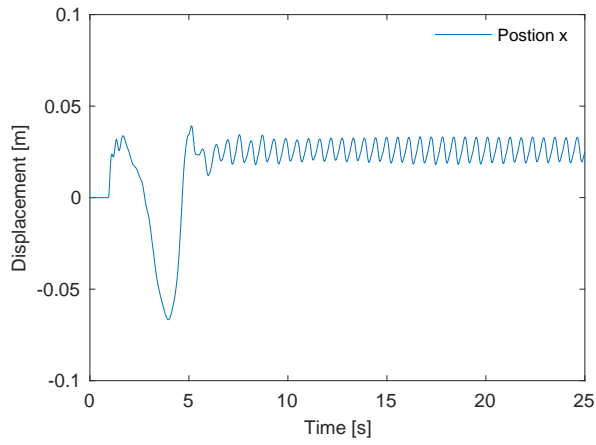
(b) Vertical position first link.

(c) Horizontal position second link.
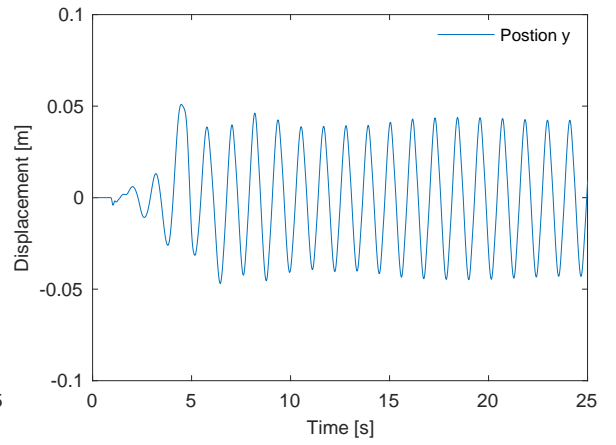
(d) Vertical position second link.
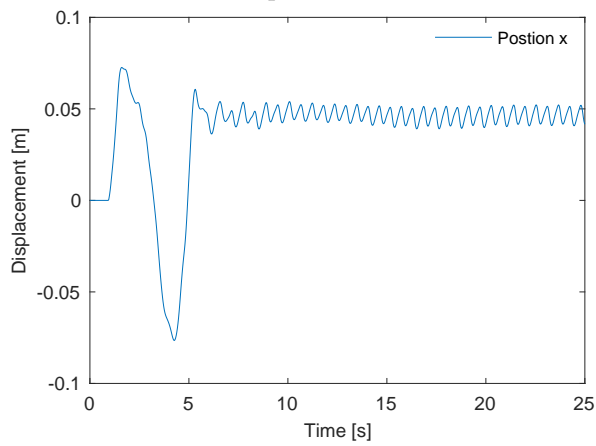
(e) Horizontal position third link.
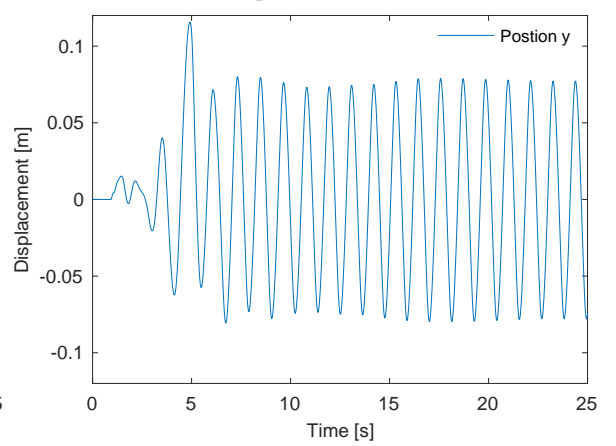
(f) Vertical position third link.

Figure 7.9: Positions and velocities of the MTLS

(a) Rotation of first link

(b) Angular velocity of first link

(c) Rotation of second link

(d) Angular velocity of second link

(e) Rotation of third link

(f) Angular velocity of third link
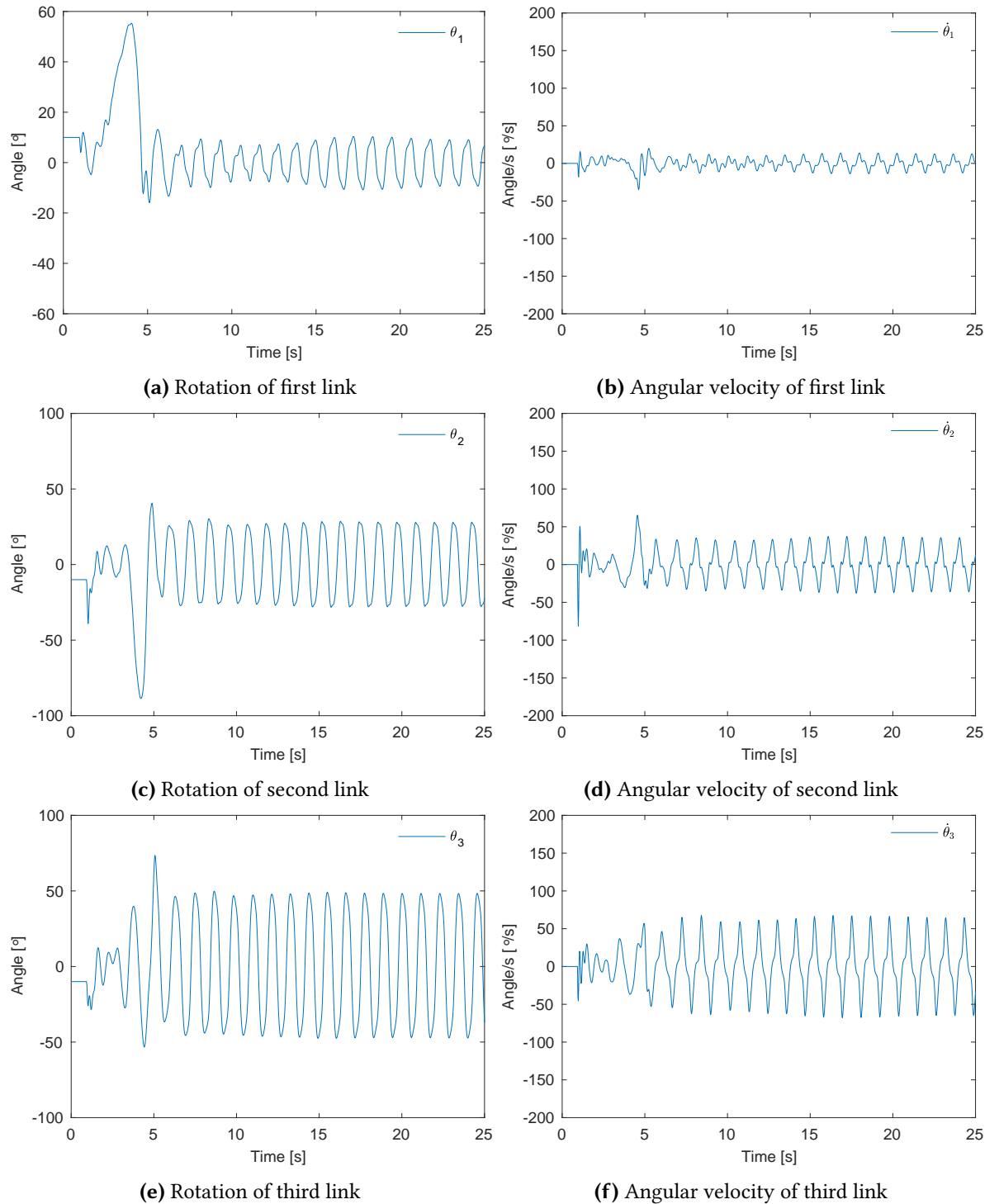
Figure 7.10: Rotations and angular velocities of the MTLS

(a) Relative rotations between first and second link.

(b) Relative angular velocities between first and second link.

(c) Relative rotations between second and third link.

(d) Relative angular velocities between second and third link.
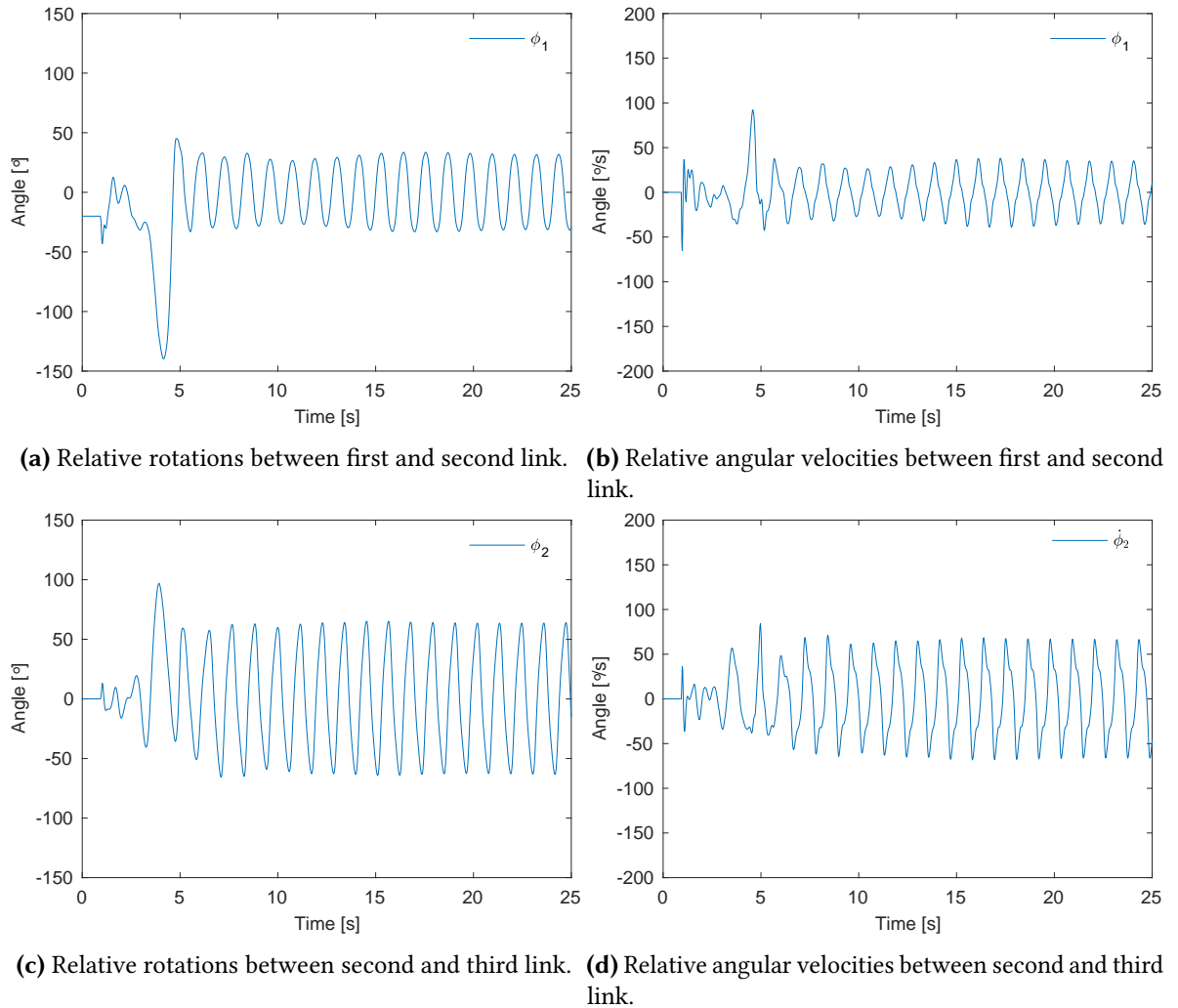
Figure 7.11: Relative rotations and relative angular velocities of the MTLS

7.7 Discussion

This section discusses the results of the work. First the differences between the computational times are evaluated, then the differences in how the models interact with the fluid are assessed. Then the energy harvesting differences are studied. Finally the limitations of the simulations are discussed.

7.7.1 Computational time

The spring used to constrain the horizontal motion of the DP was given a high spring constant. This allowed the horizontal motion to oscillate about zero with a relatively

small amplitude when compared to the vertical motion. However, this resulted in stiff dynamics, which typically leads to long computational times. This might be why the simulation time of the DP is much longer than the other simulations, as seen in table 7.1. The sharp edges of the links in the DP resulted in very high velocities at the boundary between the corner and the fluid, which often resulted in the solver not converging. To mitigate this, smoother links could be used, as was done in the BSD and TLS.

The BSD also has a very stiff spring attached to constrain the horizontal motion, however the computational times are much shorter. This might be a result of the rounded corners of the square block, which allows for a smoother transition along the boundary between fluid and solid, and allows for the use of a coarser mesh, which reduces the computational time. The BSD is constrained in the vertical direction, with the spring and damper that are attached to harvest energy. Comparing the vertical displacement of the DP in fig. 7.1 with the BSD in fig. 7.3, it is observed that the DP moves much more than the BSD. The DP has more surface area than the BSD, resulting in more interaction between the DP and the fluid as seen in figs. 7.8a–7.8d. This might also be a reason for the simulation time being much longer.

The TLS also has a short simulation time when compared to the DP, and is similar to BSD. The simulation is simplified by removing the spring and damper connection to the cylinder, which removes some of the stiff dynamics from this system. However, the TLS has a larger surface area than the BSD, and two additional rotational springs and dampers, which is why the mesh cant be coarser. By using ellipses instead of rectangles for the links, there are no sharp points where the fluid velocity approaches infinity. It is also observed that the vertical displacements of the second and third links in fig. 7.5 are significantly smaller than for the DP which results in less disruption of the wake, this can also be seen by inspecting fig. 7.8.

7.7.2   Fluid interaction

In fig. 7.8 it can be seen how the wake shape changes with the different submerged objects. The development of vortices happens closest to the cylinder for the DP, most likely this is a result of the instabilities which are induced when the DP moves through the fluid. The fast movement and large vertical displacements change where the vortex shedding occurs. There are less disruptions in the wake for the BSD, this is probably because of the more limited vertical motion. However, small local changes in the velocity field can be seen close to the boundary between the solid and fluid, indicating that the submerged object geometry affects how the fluid propagates close

to the boundary layer.

In contrast to the DP, the TLS extends the distance beween the cylinder and the vortices shed. The vortices are shed at about $x = 0.6$ m, while for the DP and BSD the shedding happens at approximately $x = 0.3$ m and $x = 0.4$ m. The constrained motion of the TLS results in less disruption of the wake, which affects how early the vortices are shed. Due to the small displacements of the TLS it acts as a splitter plate and suppresses the vortex shedding. Splitter plates are a form of passive control used to extend the wake region behind a bluff body, and reduce the pressure drag forces in the wake. This is used in the oil industry to reduce vortex induced vibrations on vertical pipes and consequently fatigue of the pipes due to the vibrations. Different thicknesses of plitter plates and distances between the bluff body and splitter plate are tested in Akilli et al. (2005). The results indicate that when the distance is larger than $2D$, where D is the diameter of the cylinder, no suppression of the vortex wake was observed. Placing the TLS further away from the cylinder might have resulted in more motion in the joints and more energy dissipation. The suppression effect might also be used to reduce the drag forces affecting the swimmer, to avoid damage on the mechanical system if this becomes a problem. However, it is not known if the AIAUV will be able to suppress the wake when it operates in a turbulent three-dimensional environment.

7.7.3 Energy harvested

By inspection of fig. 7.2, fig. 7.4, and fig. 7.7 it is apparent that the energy dissipated in the dampers in all the systems is increasing steadily. However, there are big differences in the amount for each system. The total energy dissipated in the rotational damper of the DP is approximately 10000 times larger than the linear damper of the BSD. This might be a result of the larger surface area that interacts with the fluid and leads to bigger vertical oscillations for the DP as seen in fig. 7.1b and fig. 7.1d when compared to the BSD in fig. 7.3b. The angular velocity of the DP in fig. 7.1e is also much higher than the vertical velocity of the fig. 7.3d. Comparing the linear and rotational dampers might not be practical either, due to the differences in how they work and interact with the solid. For the purposes of this thesis, investigating the energy harvesting capability of the rotational dampers is of more interest.

The TLS also has much higher energy dissipated in both dampers when compared to the BSD as seen in fig. 7.7. However, it is lower than the DP. By inspecting the angular velocity plots for the DP and TLS given in fig. 7.1f, fig. 7.6b and fig. 7.6d, it is apparent that the DP moves much faster. The maximal relative angular velocity

of the first damper and second damper in the TLS are approximately 200 deg/s and 80 deg/s, while the DP has a upper limit of 1200 deg/s. This difference in rotational velocity is likely a result of the constrained first link, which reduces how freely the TLS can move, and the reduced drag due to the vortex suppression as discussed in section 7.7.2.

The difference in the amount of energy harvested by the two dampers in the TLS is reflected in the angular velocities, where ϕ_1 is approximately twice the size of ϕ_2. The increase in energy harvested is substantially higher than the increase in velocity, which agrees with the relationship between angular velocity and energy dissipation in dampers in eq. (4.4).

7.7.4   Limitations of the simulations

An important limitation in the simulations studied is that they are all in two-dimensions. As a consequence it is possible that the AIAUV interacts with the fluid differently than in the simulations. The Reynolds number for the simulations shown is approximately 55000 which is far above the threshold for a turbulent wake, and because only the laminar modules were used for these simulations there will most likely be changes in how the wake evolves. Furthermore the AIAUV consists of different materials, unlike the submerged objects in these simulations which are made of uniform stainless steel. Furthermore the AIAUV is not necessarily constrained with an anchor, and actuators have to be used to maintain a desired distance to the cylinder, which also changes how the AIAUV interacts with the fluid when compared to the passive systems in this simulation study.

The size of the models implemented are also significantly smaller than the AIAUV, and increasing the size of the system will likely also require a larger wake and higher fluid velocities.

The energy harvesting capabilities of the AIAUV will be affected by the size difference, where larger hydrodynamic forces will be required to achieve an oscillating motion. Furthermore it is not realistic that the AIAUV will be able to move as fast as the models simulated, especially the DP has angular velocities which exceed what would be possible with the AIAUV.

7.7.5   Comparison the simulation methods

By observing the plots of all the swimmers, it is evident that the frequency of the vortex shedding is much higher for the COMSOL models. It was observed by Strouhal (1878), that the frequency of vortex shedding increases as the fluid velocity

is increased. This applies for the simulations presented, where the COMSOL models use $U_\infty = 2$ m/s and the second simulator uses $U_\infty = 0.8$ m/s.

There are similarities in the horizontal displacement for the DP, BSD and MTLS as seen in fig. 7.9, fig. 7.3 and fig. 7.1, where all the models oscillate about a value close to 0 m, after the wake has formed. However, there are large displacements observed for both the BSD and the MTLS that are not present for the DP. This might be due to the pendulum being much larger than the BSD, and the MTLS consists of three bodies that are not physically attached with a hinge, making it easier to move each individual body. Furthermore, the MTLS is neutrally buoyant, meaning that it weighs the same as the surrounding fluid, while the DP is made of stainless steel, which is much heavier, and therefore more force is required to move the DP. The constrained horizontal motion of the TLS is very different from all the other models, and is therefore disregarded when comparing horizontal displacement. It is also observed that the vertical displacements for all the models are similar. The most distinct plot is that of the BSD, where the vertical displacement oscillates faster when compared to the other COMSOL models as expected, due to the vertical spring and damper. The similarities observed for both the horizontal and vertical displacement suggest that the results are reliable.

The relative angles of the MTLS in fig. 7.11 are significantly larger than both the TLS and DP, which is mostly likely a result of the rotational springs used for the COMSOL models. The modular design and weight of the MTLS also means that less force is required to move the bodies around. However, the relative angular velocity of the MTLS is much smaller, especially when compared to the DP. This might be a result of the much slower shedding frequency, resulting in the DP experiencing a force that varies much faster than for the MTLS. However, the DP also has a rotational damper, that should have resulted in a lower angular velocity. This together with the previously stated convergence problems for the DP, suggests that further studies have to be conducted to investigate whether this is due to a bug in the implementation. The TLS has relative angular velocity that is significantly lower that that of the DP, however, it is not properly placed in the wake, due to the suppression effect discussed earlier. It is believed that placing the TLS further downstream from the cylinder would result in much higher angular, which would imply that the difference in shedding frequency is the reason for the contrast in angular velocity.

The cases studied in this thesis are limited in scope, and to properly investigate the reliability of the COMSOL simulation models, a more thorough investigation would have to be performed. Implementing the same model in both COMSOL and a

second simulator would allow for a better evaluation of the results.

Chapter 8

Position hold simulation study

In this chapter the position hold algorithm developed in chapter 6 is studied through three case studies. First the setup of the model is presented, then the cases studied are described and the results from the simulations are presented. Finally the results are discussed.

8.1 Simulation setup

The simulation is very sensitive to the choice of parameters. In this thesis the controller was tuned by changing the values and inspecting how the simulation responds until a satisfactory performance was obtained. The parameters for the control system presented in section 6.2 are chosen as shown in table 8.1.

Parameter	Value
k_ϕ	20
k_{v_ϕ}	5
α	30°
δ_{ϕ_0}	50°
λ_1	$5.26 \cdot 10^{-8}$
λ_2	0.0120
k_θ	0.07

Table 8.1: Parameters for the control system.

The parameters for the horizontal position hold controller presented in section 6.4

and the ILOS guidance law presented in section 6.3 are chosen as shown in table 8.2, where n is the number of links and l is the length of each link. To constrain the relative angle between the links and uphold assumption 6.2, a saturation of $\phi_{\max} = 20°$ is added to the links. Furthermore, the initial position for all cases was chosen to be $P_0 = [-2, 1]^T$ and all link angles are chosen to be 0.

Parameter	Value
Δ	$2\,n\,l$
δ	0.012
K_{p_ω}	2.5
K_{d_ω}	0.9
K_{i_ω}	1.5

Table 8.2: Parameters for ILOS guidance law and position hold controller

In order to test the controller, each case study has a different disturbance and/or target position. Each case will be described before the results are presented in the next sections.

8.2   Case 1 - Horizontal current

The position hold controller is intended to hold a desired position in the wake of a bluff body. In the first case it is investigated how the controller handles constant disturbances in the horizontal direction. In practice this would be similar to a symmetric wake without vortex shedding, which implies $Re < 40$. The initial state of the system is given in section 8.1, the disturbance is selected to be $V_x = -0.3$ m/s and the desired position is given by $P_1 = [35, 3]^T$.

The horizontal and vertical positions given in figs. 8.1a–8.1b shows that the trajectory converges to the desired position. The vertical position has a overshoot of approximately 0.2 m, and oscillates with an amplitude of approximately 0.01 m. Due to the undulating motion of the snake some oscillations are expected. The horizontal position overshoots by approximately 0.003 m, which is very small and might be neglected due to numerical inaccuracies when simulating. The horizontal position slowly converges to the desired position over approximately 1000 s as seen in fig. 8.1a. The overshoots in horizontal position can also be seen on the zoomed in trajectory plot fig. 8.1d, where the USR goes past the desired position, but then slows down as

seen when inspecting the relative forward velocity plot in fig. 8.3, which allows the current to push it back to the desired position. It is also observed that the desired heading is achieved in fig. 8.2, by inspecting a close up of the heading, it is seen that there is a very small offset between the measured and desired headings. However, the controller is developed with a simplified model, and some inaccuracies are expected.
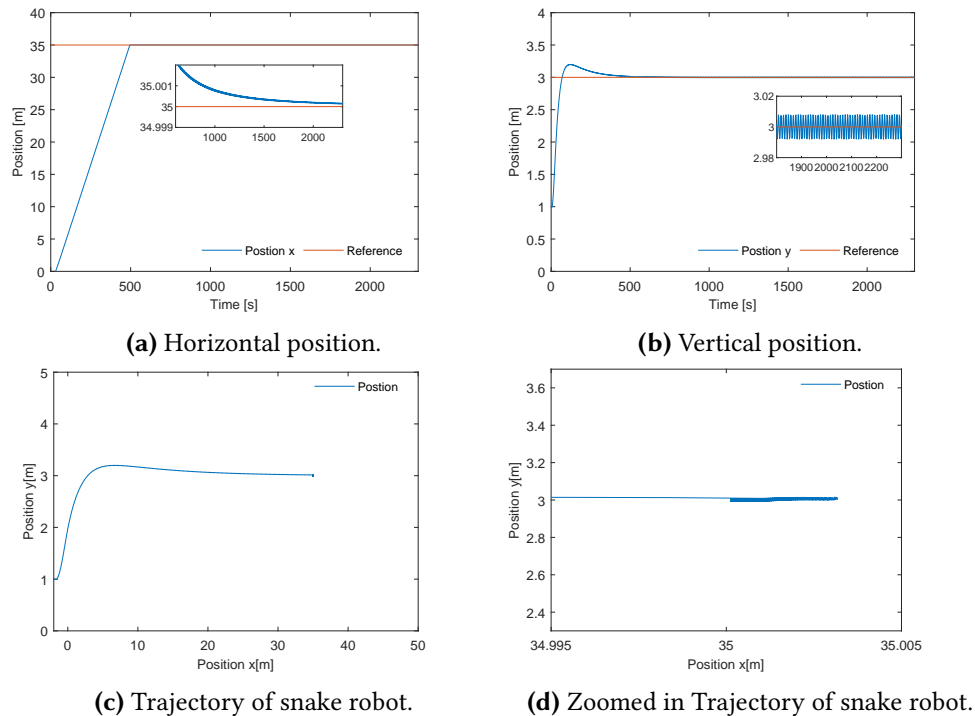

(a) Horizontal position.

(b) Vertical position.

(c) Trajectory of snake robot.

(d) Zoomed in Trajectory of snake robot.

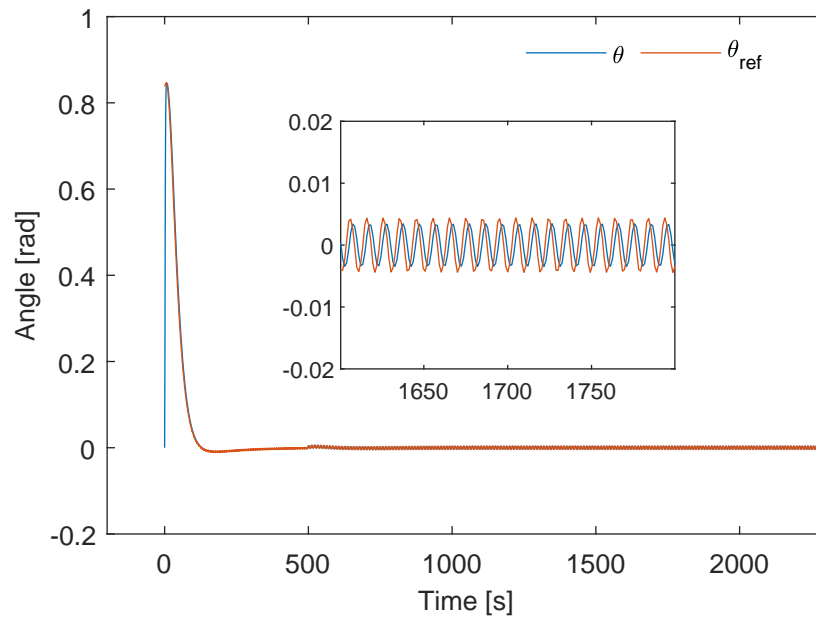**Figure 8.1:** Positions of the snake robot in case 1.

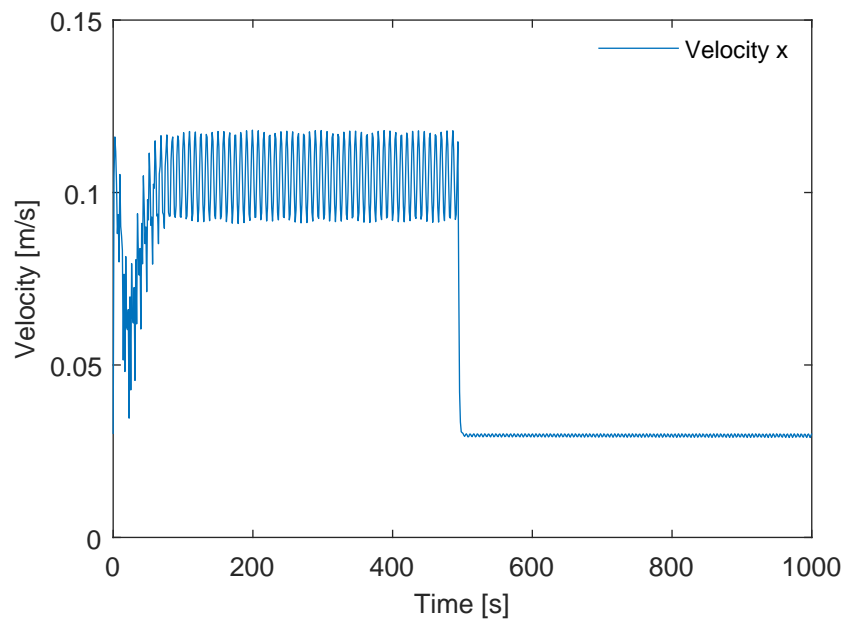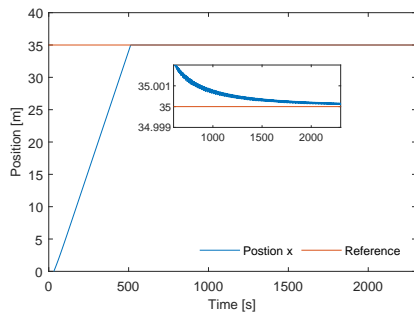**Figure 8.2:** Heading of snake robot in case 1.

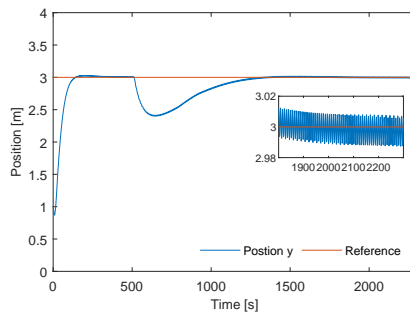**Figure 8.3:** Relative forward velocity of snake robot in case 1.

8.3 Case 2 - Constant current

The forces in the wake of a bluff body will be both horizontal and vertical. In this section the results of a simulation with constant horizontal and vertical currents are presented. The currents are selected to be $V_x = -0.3$ m/s and $V_y = -0.2$ m/s, while the desired position is the same as in section 8.2.

The horizontal position in fig. 8.4a converges to the desired value, with an overshoot of approximately 0.003 m. In contrast, the vertical position drops suddenly at 500 s, and converges to a similar value to the previous case study, albeit with some small osciallations. This drop in vertical position can also be seen in the trajectory plots figs. 8.4c−8.4d and the velocity plot fig. 8.6. Similarly to the results presented in section 8.2, the trajectory passes the desired horizontal position and slows down, while simultaneously dropping 0.4 m, after which it slowly approaches the desired position.
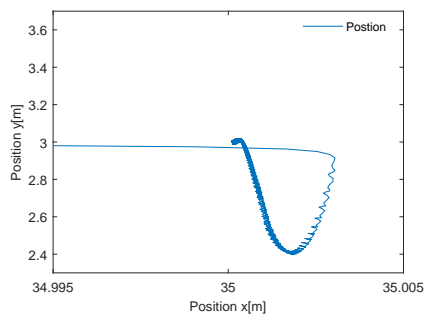

(a) Horizontal position.

(b) Vertical position.
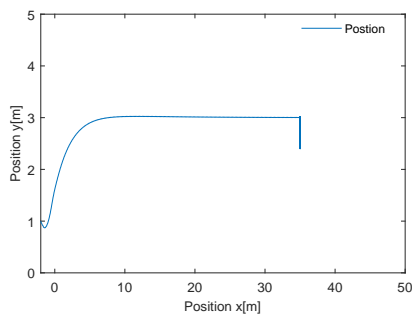
(c) Trajectory of snake robot.

(d) Zoomed in Trajectory of snake robot.

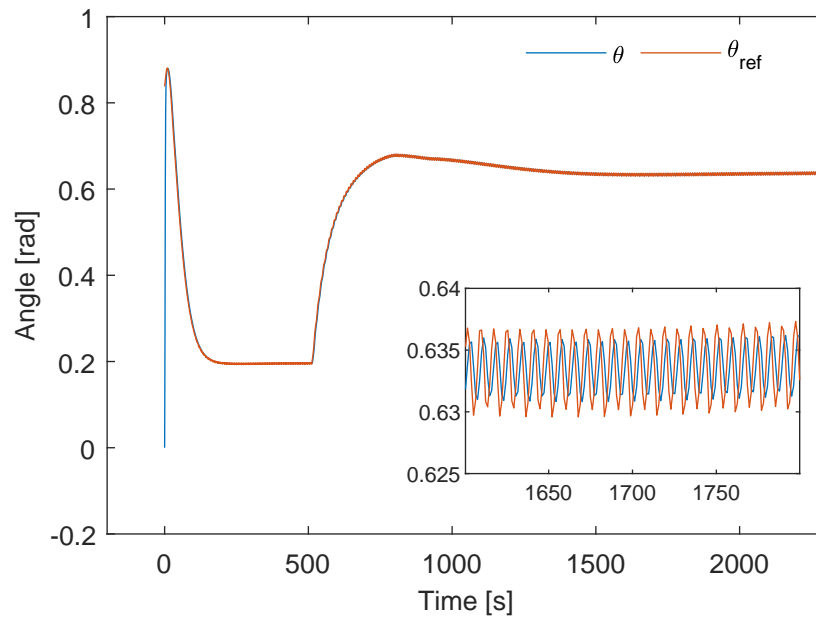**Figure 8.4:** Positions of the snake robot in case 2.

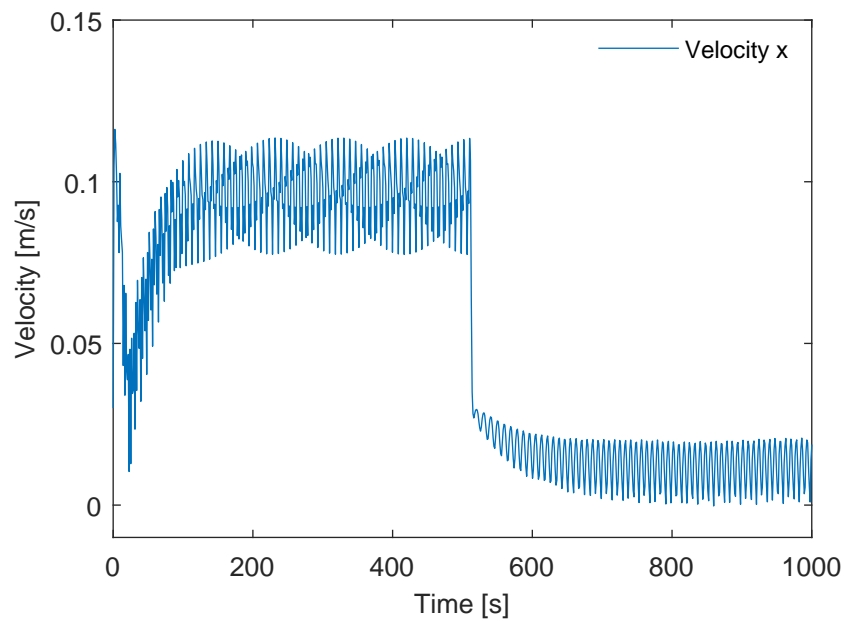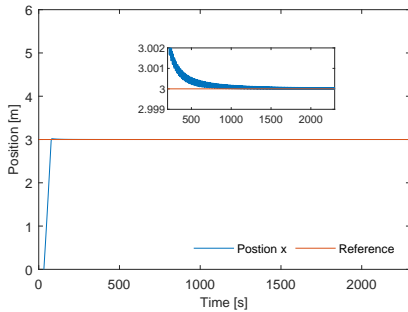**Figure 8.5:** Heading of snake robot in case 2.

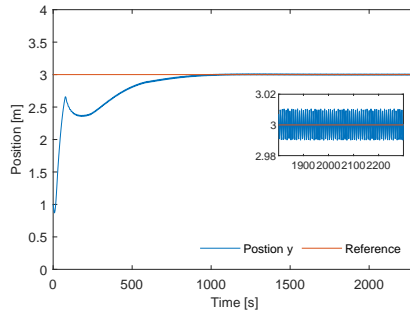**Figure 8.6:** Forward velocity of snake robot in case 2.

8.4 Case 3 - Reaching horizontal position first

In the previous case it was observed that the forward velocity starts decreasing rapidly as the USR reaches the desired horizontal position. In this case, it is investigated if the USR can reach the desired vertical position, if first reaches the desired horizontal position. The disturbances are the same as presented in section 8.3, and the desired position is chosen to be $P_3 = [3, 3]^T$.

Similarly to the previous cases, the horizontal position converges with a small overshoot of approximately 0.003 m. Unlike the results in section 8.3 however, the desired vertical position is not reached before the velocity decreases as seen in fig. 8.7b and fig. 8.9, but slowly approaches the desired values afterwards, and oscillates with an amplitude of 0.01 m about this. The trajectory is similar to that presented in section 8.3, where the desired position is reached, but the climb of the USR in vertical direction is longer.

(a) Horizontal position.

(b) Vertical position.
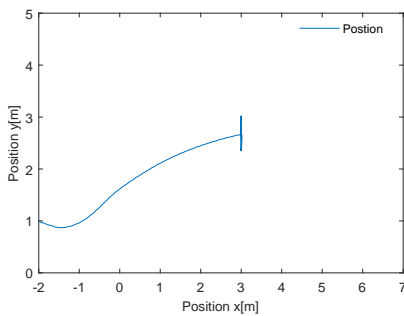
(c) Trajectory of snake robot.

(d) Zoomed in Trajectory of snake robot.

Figure 8.7: Positions of the snake robot in case 3.

Figure 8.8: Heading of snake robot in case 3.

Figure 8.9: Forward velocity of snake robot in case 3.

8.5   Discussion

In this section the results are compared and the limitations of the work are discussed.

8.5.1 Differences between the cases and convergence to desired path

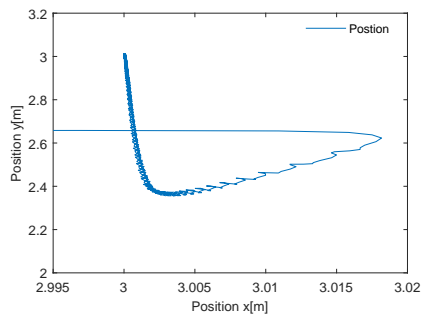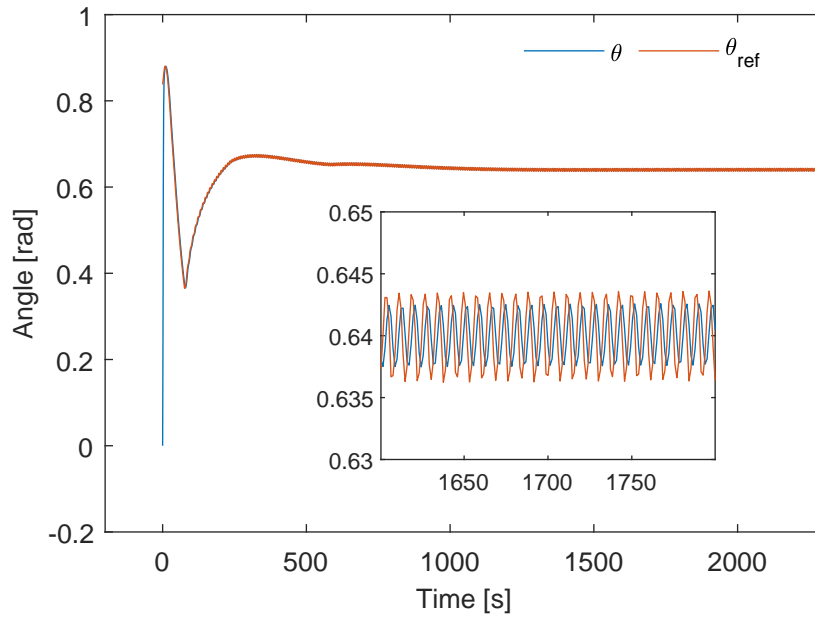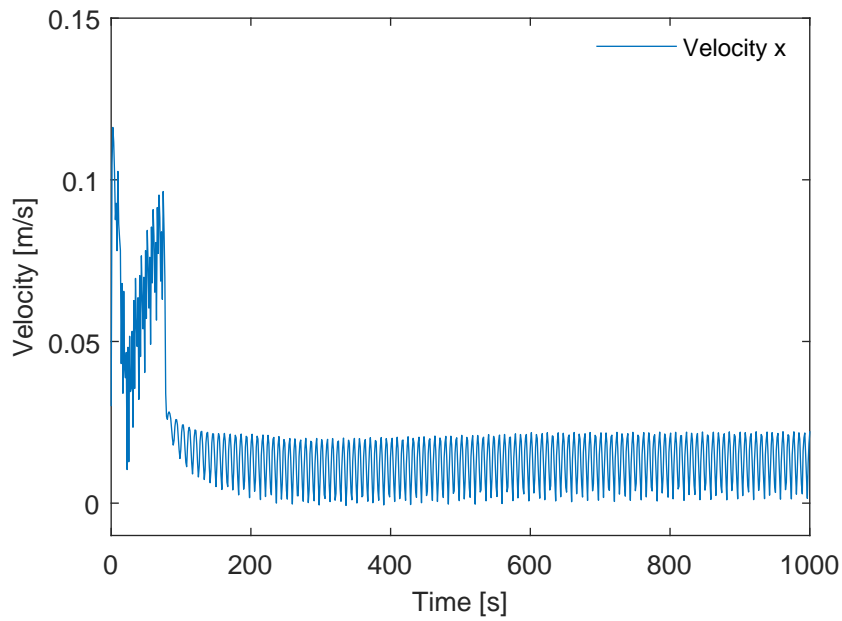As presented in the case studies, control objectives were fulfilled in all cases. However, large differences in the USR's behavior could still be observed in the different cases. There was a small overshoot in horizontal position for all the cases, which is believed to be a result of numerical inaccuracies or poor tuning. However, the overshoot is very small and poses no issues. Most of the differences can be seen in the vertical trajectory of the robot. The studies with disturbances in vertical direction show a sharp drop in vertical position as the USR arrives at the desired horizontal position. This is most likely due to the PID controller as described in section 6.4, which results in decreasing forward velocity as the USR approaches the desired horizontal position. When the speed falls, the ILOS guidance law has to readjust to the changing forward velocity, while the current drags the USR with it. This sudden decrease in velocity also leads to differences in how quickly the trajectory converges. For the first case, the vertical position is achieved in less than 600 s, while the second and third case in fig. 8.4b and fig. 8.7b seem to almost converge in about 300 s, but as the velocity drops and the controller adjusts, it slowly converges over the next 700 s. This can lead to big problems when to controller operates in the wake of a bluff body, where there are sudden changes happening to the vertical disturbances as vortices pass. It is possible that if the controller's convergence time to counteract these sudden changes is too slow, the USR could fall out of the wake, and a lot of energy would be lost as it gets back to the desired position.

A possible solution to this problem is to increase δ in eq. (6.18), which increases the integral effect of the ILOS guidance law. This would result in the controller adapting faster to changes. However, it is limited how quickly the USR can respond due to physical limitations. Changing the tuning of the PID controller can also be a good approach, so changes in forward velocity happen less abruptly. This can be done by increasing the damping coefficient and lower the integral and proportional coefficients. However, the controller does adjust to the changes slowly and the desired position is achieved. This is true for the third case as well, where the robot reached the desired horizontal position long before the vertical position was achieved. However, increasing the vertical current too much will result in large θ_{ref} values, which violates assumption 6.2 and it is uncertain how the system will behave under such circumstances. Furthermore, studying how the controller handles changes in the reference values after reaching the desired position, might also be interesting due to the abrupt changes in velocity.

8.5.2   Limitations

During the development of the simplified model and controller some assumptions were made, in particular assumption 6.3, where it was assumed that the currents were irrotational and constant. This is very different from the wake of a bluff body were the disturbances are highly rotational and varying. Testing the robustness of this controller with a simulation that also captures the FSI coupling and vortex street effects is necessary to evaluate if it is robust enough, and it is possible that further development is needed to achieve a satisfactory performance. The results presented in this chapter indicate that the controller will work under certain conditions, with constant disturbances that are not too big for the forward motion of the USR to overcome. However, the forces in the wake might be too large for forward propulsion by using just the undulation and small link angles, implying that thrusters available on the AIAUV would necessary to properly take advantage of the energy in a vortex street.

To evaluate if the controller presented in this study also applies to a AIAUV in the wake of bluff bodies, a larger case study has to be performed, with more varied cases and simulators that can capture the FSI between the AIAUV and vortex street. The three cases investigated in this chapter only consider three specific cases with certain currents. Performance in other situations can't be properly assessed without a more thorough study and theoretical evaluation. In this thesis no theoretical proof for this method has been derived, which also increases the need for a proper extensive case study.

Chapter 9

Conclusion and future work

In this chapter a conclusion based on the work in this thesis is presented, then future work is suggested.

9.1 Conclusion

The equations of motion for 4 models are derived and presented: a double pendulum connected to a cylinder with a spring and damper, a square connected to a cylinder and the lower end wall with springs and dampers, a three link swimmer where the first link is immovable, and a three link swimmer where the links are connected by springs and the first link is connected to a cylinder. The first three models were implemented in COMSOL Multiphysics and the fourth model was implemented in the simulator presented by Gazzola et al. (2011). The simulations showed that all the models harvested energy, but the total energy harvested varied from 2.5 J in 25 s for the BSD to 32000 J in 20 s for the DP. Furthermore, the DP and first link of TLS had angular velocities that far exceeded what would be physically possible with an USR or AIAUV, which suggests that further investigation is needed to assess how well energy can be harvested for more realistic swimmers. The FSI for the models also seemed to vary, where the large displacements and high angular velocities of the DP created more disruptions in the wake, while the constrained motion of the TLS led to small displacements which resulted in an elongated distance between the cylinder and the vortices being shed, suggesting that it acts similarly to a splitter plate.

The use of rectangles when modelling the DP led to sharp angles where the fluid velocity goes to infinity, which resulted in long computational times and converging issues. This was improved in the BSD and TLS by using rectangles with smoothed edges and ellipses, which allowed for faster simulations, and fewer crashes.

The fourth model was implemented with a different solver than the other models. This simulator was developed in Gazzola et al. (2011) and verified through well known simulation studies. The results from both simulation methods were compared to assess how reliable the results are. The horizontal and vertical displacements are similar for all models, suggesting that they are reliable. However, the angular velocities are very different for the models. This might be a result of the difference in shedding frequency for the two simulation methods, but further studies are required before the reliability of these results can be evaluated.

Furthermore, a position hold controller was developed by using the simplified control oriented model for USRs developed in Kelasidi, Pettersen and Gravdahl (2014), later extended to include currents in Kohl et al. (2015b) and Kohl et al. (2015a), and the ILOS guidance law implemented in Kohl et al. (2016). The performance of the controller was assessed through three simulation studies, which suggested that in the presence of constant disturbances, the controller achieved the desired position. However, only three cases were investigated, and the controller is intended for usage downstream in the wake of a cylinder in the presence of a vortex shedding where disturbances are rotational and varying with time. To investigate whether the controller can be used in such an environment, further studies are needed. The controller was also shown to perform badly in the presence of vertical disturbances, due to the structure of the controller the forward velocity would decrease quickly as the desired position was approached. While the ILOS guidance law managed to adapt to the changes, it was slow which resulted in the USR drifting away from the desired position before moving back.

9.2   Future work

In this section future work is suggested.

- **Study energy harvesting of articulated swimmers:** To further investigate the energy harvesting capacities of USRs and AIAUVs, simulations with FSI and articulated swimmers have to be developed and studied, this might be done by following a similar approach to Bernier et al. (2018).

- **Extend simulations to three dimensions and turbulent environments:** By extending the simulations to a turbulent three-dimensional environment more realistic cases can be studied, which allows for a better view of how the AIAUV can harvest energy and how it will interact with the wake of a bluff body.

- **Theoretical analysis of position hold controller:** The position hold controller developed in this thesis has not been theoretically assessed and the stability of the method has not been proven. By performing a proper analysis the limits of the controller might be easier to evaluate, and improvements can be made to make a more robust controller.

- **Further simulation studies of the position hold controller:** By performing several more diverse simulation studies of the controller, new insight might be gathered for how the controller can be improved. Furthermore, case studies with time-varying rotational disturbances is necessary before the usability of the controller in presence of vortex shedding can be evaluated.

- **Testing different parameters for the position hold controller:** Different parameters might yield a better performance for the position hold controller. By increasing the integral effect of the ILOS guidance law controller, a faster response to the falling velocity might be achieved, and the overshoot present in the results might be reduced.

Appendix A

Appendix A - Simulation models

A.1   Jacobians of MTLS

The jacobians are given by the following matrices:

$$J_1(\varphi) = \begin{bmatrix} \cos\theta_1 & \sin\theta_1 & 0 & 0 & 0 & 0 & 0 & 0 & 0 \\ -\sin\theta_1 & \cos\theta_1 & 0 & 0 & 0 & 0 & 0 & 0 & 0 \\ 0 & 0 & 1 & 0 & 0 & 0 & 0 & 0 & 0 \end{bmatrix}, \tag{A.1}$$

$$J_2(\varphi) = \begin{bmatrix} 0 & 0 & 0 & \cos\theta_2 & \sin\theta_2 & 0 & 0 & 0 & 0 \\ 0 & 0 & 0 & -\sin\theta_2 & \cos\theta_2 & 0 & 0 & 0 & 0 \\ 0 & 0 & 0 & 0 & 0 & 1 & 0 & 0 & 0 \end{bmatrix}, \tag{A.2}$$

$$J_3(\varphi) = \begin{bmatrix} 0 & 0 & 0 & 0 & 0 & 0 & \cos\theta_3 & \sin\theta_3 & 0 \\ 0 & 0 & 0 & 0 & 0 & 0 & -\sin\theta_3 & \cos\theta_3 & 0 \\ 0 & 0 & 0 & 0 & 0 & 0 & 0 & 0 & 1 \end{bmatrix}, \tag{A.3}$$

where $c_1 = \cos(\theta_1 + \phi_1)$, $s_1 = \sin(\theta_1 + \phi_1)$, $c_2 = \cos(\theta_1 + \phi_1 + \phi_2)$ and $s_2 = \sin(\theta_1 + \phi_1 + \phi_2)$.

References

Akilli, H., Sahin, B. and Tumen, N. F. (2005). Suppression of vortex shedding of circular cylinder in shallow water by a splitter plate, *Flow Measurement and Instrumentation* **16**(4): 211–219.

Allen, J. J. and Smits, A. J. (2001). ENERGY HARVESTING EEL, *Journal of Fluids and Structures* **15**(3-4): 629–640.

Bernier, C., Gazzola, M., Chatelain, P. and Ronsse, R. (2018). Numerical simulations and development of drafting strategies for robotic swimmers at low reynolds number, *2018 7th IEEE International Conference on Biomedical Robotics and Biomechatronics (Biorob)*, IEEE.

Bernier, C., Gazzola, M., Ronsse, R. and Chatelain, P. (2019). Simulations of propelling and energy harvesting articulated bodies via vortex particle-mesh methods, Vol. 392, Elsevier BV, pp. 34–55.

Borhaug, E., Pavlov, A. and Pettersen, K. Y. (2008). Integral LOS control for path following of underactuated marine surface vessels in the presence of constant ocean currents, *2008 47th IEEE Conference on Decision and Control*, IEEE.

COMSOL (2019). *COMSOL Multiphysics Reference Manual 5.5*, COMSOL AB.

Coquerelle, M. and Cottet, G.-H. (2008). A vortex level set method for the two-way coupling of an incompressible fluid with colliding rigid bodies, *Journal of Computational Physics* **227**(21): 9121–9137.

Eldredge, J. D. (2006a). Numerical simulation of the fluid dynamics of 2d rigid body motion with the vortex particle method, *Journal of Computational Physics* **221**(2): 626–648.

Eldredge, J. D. (2006b). Numerical simulations of undulatory swimming at moderate reynolds number, *Bioinspiration & Biomimetics* **1**(4): S19–S24.

Eldredge, J. D. and Pisani, D. (2008). Passive locomotion of a simple articulated fish-like system in the wake of an obstacle, *Journal of Fluid Mechanics* **607**: 279–288.

Ferziger, J. H. and Perić, M. (1999). *Computational Methods for Fluid Dynamics*, Springer Berlin Heidelberg.

Fossen, T. I. (2011). *Handbook of marine craft hydrodynamics and motion control*, John Wiley & Sons.

Gazzola, M., Chatelain, P., van Rees, W. M. and Koumoutsakos, P. (2011). Simulations of single and multiple swimmers with non-divergence free deforming geometries, *Journal of Computational Physics* **230**(19): 7093–7114.

Henderson, R. (2006). Design, simulation, and testing of a novel hydraulic power take-off system for the pelamis wave energy converter, *Renewable Energy* **31**(2): 271–283.

Kelasidi, E., Pettersen, K. Y. and Gravdahl, J. T. (2014). A control-oriented model of underwater snake robots, *2014 IEEE International Conference on Robotics and Biomimetics (ROBIO 2014)*, IEEE.

Kelasidi, E., Pettersen, K. Y., Gravdahl, J. T. and Liljeback, P. (2014). Modeling of underwater snake robots, *2014 IEEE International Conference on Robotics and Automation (ICRA)*, IEEE.

Kohl, A. M., Kelasidi, E., Pettersen, K. Y. and Gravdahl, J. T. (2015a). Analysis of underwater snake robot locomotion based on a control-oriented model, *2015 IEEE International Conference on Robotics and Biomimetics (ROBIO)*, IEEE.

Kohl, A. M., Kelasidi, E., Pettersen, K. Y. and Gravdahl, J. T. (2015b). A control-oriented model of underwater snake robots exposed to currents, *2015 IEEE Conference on Control Applications (CCA)*, IEEE.

Kohl, A. M., Kelasidi, E., Pettersen, K. Y. and Gravdahl, J. T. (2016). Planar path following of underwater snake robots in the presence of ocean currents, *IEEE Robotics and Automation Letters* **1**(1): 383–390.

Liljeback, P., Haugstuen, I. U. and Pettersen, K. Y. (2012). Path following control of planar snake robots using a cascaded approach, *IEEE Transactions on Control Systems Technology* **20**(1): 111–126.

Liljebäck, P., Pettersen, K. Y., Stavdahl, Ø. and Gravdahl, J. T. (2013). A simplified model of snake robot locomotion on planar surfaces, *Snake Robots*, Springer London, pp. 103–129.

Markaroglu, H., Guzelkaya, M., Eksin, I. and Yesil, E. (2006). Tracking time adjustment in back calculation anti-windup scheme, *ECMS 2006 Proceedings edited by: W. Borutzky, A. Orsoni, R. Zobel*, ECMS.

Newman, J. N. (2018). *Marine hydrodynamics*, The MIT press.

Ozkop, E. and Altas, I. H. (2017). Control, power and electrical components in wave energy conversion systems: A review of the technologies, *Renewable and Sustainable Energy Reviews* **67**: 106–115.

Pepper, D. W. and Heinrich, J. C. (2017). *The finite element method: basic concepts and applications with MATLAB, MAPLE, and COMSOL*, CRC press.

Strouhal, V. (1878). Ueber eine besondere art der tonerregung, *Annalen der Physik und Chemie* **241**(10): 216–251.

Sumer, B. M. et al. (2006). *Hydrodynamics around cylindrical strucures*, Vol. 26, World scientific.

Amer Orucevic

Underwater snake robots in vortex wakes

NTNU

Norwegian University of
Science and Technology